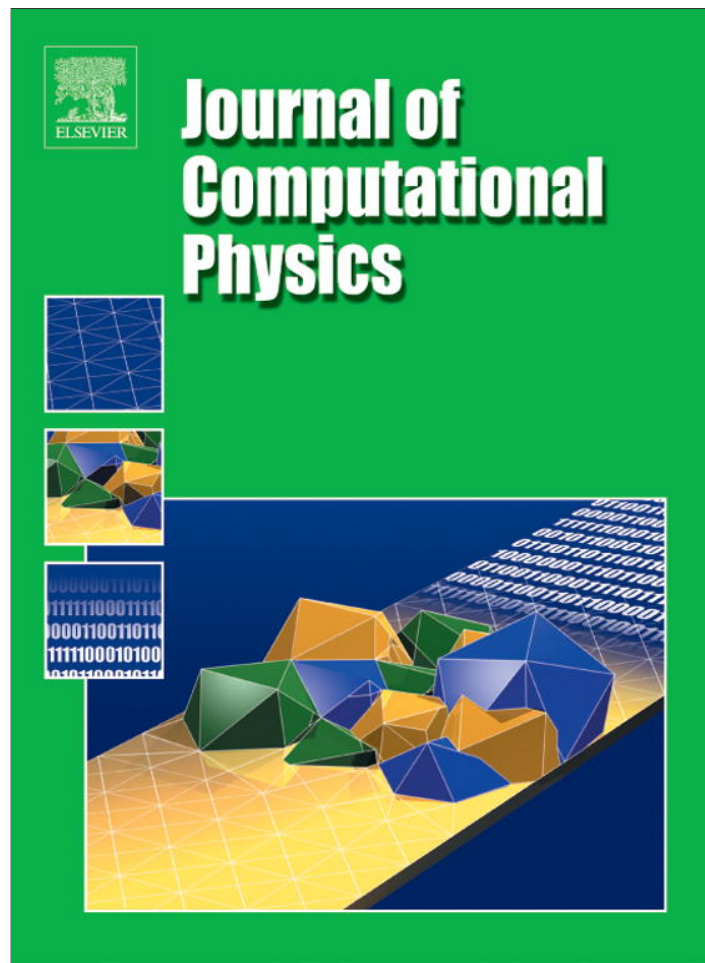


Provided for non-commercial research and education use.
Not for reproduction, distribution or commercial use.



(This is a sample cover image for this issue. The actual cover is not yet available at this time.)

This article appeared in a journal published by Elsevier. The attached copy is furnished to the author for internal non-commercial research and education use, including for instruction at the authors institution and sharing with colleagues.

Other uses, including reproduction and distribution, or selling or licensing copies, or posting to personal, institutional or third party websites are prohibited.

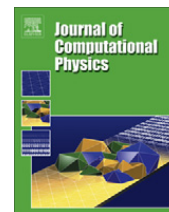
In most cases authors are permitted to post their version of the article (e.g. in Word or Tex form) to their personal website or institutional repository. Authors requiring further information regarding Elsevier's archiving and manuscript policies are encouraged to visit:

<http://www.elsevier.com/copyright>



Contents lists available at SciVerse ScienceDirect

Journal of Computational Physics

journal homepage: www.elsevier.com/locate/jcp

An Eulerian–Lagrangian moving immersed interface method for simulating burning solids



M.T. McGurn, K.P. Ruggirello, P.E. Desjardin*

Department of Mechanical and Aerospace Engineering, University at Buffalo, the State University of New York, Buffalo, NY 14260-4400, USA

ARTICLE INFO

Article history:

Received 12 May 2011

Received in revised form 1 November 2012

Accepted 30 January 2013

Available online 13 February 2013

Keywords:

Burning solids

Fluid–structure

Ghost–fluid

ABSTRACT

This study concerns the development of a numerical methodology to conduct conjugate heat and mass transfer simulations of burning and moving solids. The flow is described using an Eulerian representation and the solid described using a Lagrangian finite element (FE) method. The fluid–solid interface is defined using a level set function that is initialized by a surface mesh representation that balances accuracy with the computational cost of re-initializing moving interfaces. A ghost–fluid methodology is implemented that results in low errors in mass and energy conservation. Mass transfer from solid ablation is computed explicitly using surface integration over the solid surface mesh to guarantee enforcement of conservation principles. The introduced methodologies are applied to the study of the burning of carbon–epoxy composites.

© 2013 Elsevier Inc. All rights reserved.

1. Introduction

The origin of immersed interface methodologies has its roots in the methods developed by Peskin to simulate cardiac mechanics [1]. Since then the use of immersed interfaces for describing fluid–solid interactions has expanded greatly to examine a range of applications for incompressible [2,3] and compressible [4–7] flows. Recent reviews on the topic can be found by Osher and Fedkiw [8], and Mittal and Iaccarino [9]. The focus of the current effort is to develop an ghost–fluid based immersed boundary methodology for describing the conjugate heat and mass transfer processes associated with burning solids. The flow for these simulations is solved using Eulerian discretization approaches and the solid is solved using a Lagrangian finite element method (FE). To the authors' knowledge, this study presents the first application of ghost–fluid methodology to charring solids.

The specific application of interest is the response of polymer structures to fire environments. One of the outstanding issues in fire science is a better understanding of flame spread which is controlled by the conjugate heat and mass transfer processes at the fluid–solid interface. The heating of a combustible structural material often results in pyrolysis of the material that generates volatile gases which, in turn, burn in the surrounding air providing additional heat for further pyrolysis. While there is a rich history of modeling flame spread, the models are often limited to only providing qualitative estimates of flame spread velocity. More quantitative predictions rely on coupled simulations of mass and heat transfer processes [10,11].

The main challenge for coupling these two different numerical methods are the disparately different mesh topologies and maintaining numerical stability during the coupling. The components for a coupling scheme include: (1) an efficient and accurate update of moving interfaces, (2) the treatment of no-slip and no-penetration boundary conditions at the solid interface as viewed by the flow solver and (3) exchange of energy and mass transfer across interface. Two commonly used approaches are often applied to impose interface constraints associated with the last two items. The first approach is to

* Corresponding author. Tel.: +1 716 645 1467.

E-mail address: ped3@buffalo.edu (P.E. Desjardin).

| Nomenclature | | Greeks | |
|-------------------|--|-------------------------|--|
| a_n | interface normal acceleration (m/s ²) | α | reaction progress variable |
| C | proportionality constant | α_g | thermal diffusivity (m ² /s) |
| C_p | specific heat (J/kg K) | γ | level set function (m) |
| \mathbf{d} | distance vector (m) | Γ | surface area (m ²) |
| $D_{i,m}$ | effective binary diffusion coefficient (m ² /s) | ε | emissivity |
| e | internal energy (J/kg) | ζ | mapped coordinate |
| E | total energy (J/kg) | η | non-dimensional coordinate |
| f | body force term (m/s ²) | θ | non-dimensional temperature |
| F | safety factor | μ | molecular viscosity (Pa s) |
| \mathbf{g} | contra-variant vector (1/m) | ρ | density (kg/m ³) |
| h | enthalpy (J/kg) | $\boldsymbol{\sigma}$ | Cauchy stress tensor (Pa) |
| h | convection coefficient (W/m ² K) | $\tilde{\sigma}$ | Stefan Boltzmann constant (W/m ² K ⁴) |
| h_{py} | heat of pyrolysis (J/kg) | τ | non-dimensional time |
| H | total enthalpy (J/kg) | $\boldsymbol{\tau}$ | viscous stress tensor (Pa) |
| K | curvature | $\tilde{\varphi}$ | volume fraction |
| \mathbf{k} | thermal conductivity (W/m ² K) | Ψ | basis function |
| \tilde{K} | permeability (m ²) | ω_r | relaxation factor |
| \tilde{l} | patch level | | |
| L_s | heat of sublimation (J/kg) | Subscripts/superscripts | |
| Le | Lewis number | <i>app</i> | applied |
| m'' | mass flux, (kg/m ² s) | <i>crit</i> | critical |
| M | mass (kg) | <i>diff</i> | diffusion |
| \dot{m}''' | mass source/sink term, (kg/m ³ s) | <i>e</i> | element |
| \mathbf{n}_k | surface normal | <i>ener</i> | energy |
| Nu_L | Nusselt number | <i>exp</i> | expansion |
| p | pressure, Pa | <i>f, c, r</i> | fiber, char, resin |
| Pr | Prandtl number | <i>g, s</i> | gas, solid constituent |
| q'', \mathbf{q} | heat flux, (kW/m ²) | <i>G</i> | ghost node |
| R | radius of curvature | <i>i</i> | constituent, species |
| Re | Reynolds number | <i>int</i> | interface |
| Ra_L | Rayleigh number | <i>j</i> | element node |
| Sc | Schmidt number | <i>k</i> | interface constituent |
| St | Strouhal number | <i>LES</i> | large eddy simulation |
| Ste | Stefan number | <i>mass</i> | mass |
| t | time (s) | <i>mom</i> | momentum |
| \mathbf{t} | tangential unit vector | <i>n</i> | normal direction |
| T | temperature, (K) | <i>o, e</i> | initial, end state |
| \mathbf{u} | velocity (m/s) | <i>rad</i> | radiation |
| \mathbf{U} | momentum (kg m/s) | <i>s</i> | sublimation |
| V | volume (m ³) | <i>t</i> | tangent direction |
| \mathbf{V}^i | interface velocity (m/s) | <i>vol</i> | volumetric |
| W | weighting factor | | |
| \mathbf{x} | location vector (m) | | |
| Y | species mass fraction | | |

impose the constraints as point source forcing functions. These approaches, based on the early methodologies developed by Peskin [1], are often used in incompressible flow formulations [2] because of their relative ease of implementation when solving a Poisson equation for pressure. The second approach is a ghost-fluid approach where the interface constraints are imposed *via* specification of ghost-fluid properties by reflection and interpolation [8]. Ghost-fluid approaches are often used for compressible flow formulations for which local solutions (i.e., a Riemann solution) can be used to specify the state of the ghost-cells and can be readily adapted for use in explicit time marching schemes. For the current problem, a combination of these two approaches is found useful for developing a robust coupling algorithm for describing conjugate heat and mass transfer processes.

The rest of this study begins with a description of the governing equations and a discussion of the partitioning of various terms for solution using the level-set based immersed interface. The numerical formulation follows with details on the re-initialization of the level-set function using an adaptive surface mesh representation of moving solid interfaces, the ghost-fluid implementation, and treatment of source terms associated with the generation of pyrolysis gases due to thermal decomposition of the solid. In the results, several benchmark validation problems are first presented showing increasing lev-

els of complexity with regard to the level of coupling. Finally, 2D fully coupled simulations are presented showing the burning of carbon-epoxy composites.

2. Formulation

2.1. Eulerian model

The flow-field is described by the Navier–Stokes equations for a fully compressible, reactive gas

$$\frac{\partial \rho}{\partial t} + \nabla \cdot (\rho \mathbf{u}) = 0, \tag{1a}$$

$$\frac{\partial (\rho Y_i)}{\partial t} + \nabla \cdot (\rho Y_i \mathbf{u}) = -\nabla \cdot \mathbf{m}_i^{diff} + \dot{m}_i'', \tag{1b}$$

$$\frac{\partial (\rho \mathbf{u})}{\partial t} + \nabla \cdot (\rho \mathbf{u} \mathbf{u} + p) = \nabla \cdot \tilde{\boldsymbol{\tau}} + \rho \mathbf{f}, \tag{1c}$$

$$\frac{\partial (\rho E)}{\partial t} + \nabla \cdot (\rho \mathbf{u} H) = \nabla \cdot (\mathbf{u} \cdot \tilde{\boldsymbol{\tau}}) - \nabla \cdot \mathbf{q} + \mathbf{u} \cdot \rho \mathbf{f}, \tag{1d}$$

where $E = e + \mathbf{u} \cdot \mathbf{u}/2$ is the total energy, $H (= h + \mathbf{u} \cdot \mathbf{u}/2)$ is the total enthalpy, and \dot{m}_i'' are source or sink terms associated with chemical reactions. The viscous stress tensor ($\tilde{\boldsymbol{\tau}}$), species diffusion (\mathbf{m}_i^{diff}), and heat fluxes (\mathbf{q}), are modeled using Newton's, Fick's and Fourier's laws, respectively, with simple models of diffusion,

$$\tilde{\boldsymbol{\tau}} = \mu(T) \left(-\frac{2}{3} \nabla \cdot \mathbf{u} + (\nabla \mathbf{u} + (\nabla \mathbf{u})^T) \right) \tag{2a}$$

$$\mathbf{m}_i^{diff} = -\mu(T) \nabla Y_i / Sc \tag{2b}$$

$$\mathbf{q} = -\mu(T) (Cp(1 - 1/Le) \nabla T / Pr + \nabla h / Sc). \tag{2c}$$

The molecular Schmidt (Sc), Prandtl (Pr), and Lewis (Le) numbers are set to 1.0, 0.7, and 1.43, respectively. The molecular viscosity is assumed to depend on a Sutherland's Law, $\mu = \mu_o(T_o + S)/(T + S)(T/T_o)^{3/2}$, with constants μ_o , T_o and S set equal to 1.716×10^{-5} , 273 and 111, respectively, corresponding to air [12]. The molecular diffusivities of all species are assumed equal but may vary as a function of temperature through the dependence on the prescribed Sc number. The quantity \mathbf{f} in Eqs. (1c) and (1d) is the body force term.

To develop a ghost-fluid algorithm, a set of general interface jump conditions are considered for a moving and blowing surface,

$$[[\rho_k(\mathbf{u}_k - \mathbf{V}^l) \cdot \mathbf{n}_k]] = [[\dot{m}_k'']] = 0 \tag{3a}$$

$$[[Y_{i,k} \dot{m}_k'' + \dot{m}_{k,i}^{diff}]] = 0 \tag{3b}$$

$$[[\dot{m}_k'' \mathbf{u}_k + \tilde{\boldsymbol{\sigma}}_k \cdot \mathbf{n}_k]] = 0 \tag{3c}$$

$$[[\sum_i (\dot{m}_{k,i}'' E_{k,i}) + (\tilde{\boldsymbol{\sigma}}_k \cdot \mathbf{u}_k) \cdot \mathbf{n}_k - \dot{q}_k'']] = 0 \tag{3d}$$

where the $[[(\)]]$ notation denotes $\sum_k(\)$ where the subscript $k = g, s$ represents a property of either the gas or solid side of the interface. The quantity \mathbf{n}_k is the surface normal, \mathbf{V}^l is the interface velocity, and $\dot{q}_k'' (= k_k \nabla T_k \cdot \mathbf{n}_k)$ is the normal heat conduction. The quantity $\tilde{\boldsymbol{\sigma}}_k$ is the Cauchy stress tensor for the k th phase. The treatment of pyrolysis is described using two different modeling approaches depending on if a char layer is formed. For charring materials such as wood or thermosetting polymers, pyrolysis can be considered a volumetric phenomena and a porous media flow modeling approach is often used [13,14] (more details in Section 2.2). The solid phase of the interface in this case is actually a mixture of gas and solid char that is generated from the products of pyrolysis. For non-charring materials such as PMMA, pyrolysis may be treated as surface phenomena. In both cases, the Lagrangian model computes the extent of pyrolysis and associated amount of mass, momentum and energy transferred to the Eulerian flow (to be discussed in Section 3.2.1).

The general jump relations given in Eq. (3) are further simplified for the low Mach number case of interest. Taking (1c) \mathbf{u}_k results in,

$$(\nabla \cdot \tilde{\boldsymbol{\sigma}}_k) \cdot \mathbf{n}_k = \rho_k \left[a_{n,k} - \frac{|\mathbf{u}_{t,k}|^2}{R_k} - \mathbf{f}_k \right] \quad (4)$$

where $a_{n,k} = D(\mathbf{u}_k \cdot \mathbf{n}_k)/Dt$ is the interface normal acceleration, $R_k = 1/(\nabla \cdot \mathbf{n}_k)$ is the radius of curvature and $\mathbf{u}_{t,k}$ is the tangential velocity to the interface. Taking $\nabla \cdot (3c)$ and substituting in Eq. (4) for the solid phase, results in the following expression for gas phase normal pressure gradient,

$$\frac{\partial p_g}{\partial n_g} = \rho_s \left[\frac{|\mathbf{u}_{t,k}|^2}{R_g} - a_n + \mathbf{f} \cdot \mathbf{n}_g \right] - \frac{p_s - p_g}{R_g} - (\tilde{\boldsymbol{\sigma}}_s^D - \tilde{\boldsymbol{\sigma}}_g) : \nabla \mathbf{n}_g + (\nabla \cdot \tilde{\boldsymbol{\sigma}}_g) \cdot \mathbf{n}_g \quad (5)$$

where $a_n = D(\mathbf{u}_s \cdot \mathbf{n}_g)/Dt$ is the solid acceleration defined using the gas unit normal direction and $\tilde{\boldsymbol{\sigma}}_s^D$ is the deviatoric component of Cauchy stress tensor for the solid phase. Eq. (5) is used to populate the gas pressure in the ghost–fluid cells using an interpolation procedure (to be discussed in Section 3.2). Including only the first term on the RHS of Eq. (5) results in the same balance relation as that used in [15] who showed limited success with this type of boundary conditions for strong shock interactions. For low Mach number flows, $p_g \approx p_s$, across the interface and the second term on the RHS of Eq. (5) is identically equal to zero. For high Mach flows, however, this is not the case and may help explain some of the discrepancies discussed in [15] when a simplified version of Eq. (5) is compared to the use of a Riemann solver for populating the gas pressure in the ghost–fluid cells. For the current study, the flow is at a low Mach number and therefore the second term on the RHS of Eq. (5) is very small and is ignored. The third and fourth terms on the RHS of Eq. (5) account for the effects of viscous shear and the response of the solid to those shear forces. These terms ensure the pressure gradient is adjusted such that a no-slip condition is imposed for the tangential component of the velocity. Rather than including these terms, no-slip and no-penetration boundary conditions are explicitly enforced for populating the gas velocity in the ghost–fluid,

$$[[\mathbf{u}_k \cdot \mathbf{n}_k]] = 0 \quad (6a)$$

$$[[\mathbf{u}_k \cdot \mathbf{t}_k]] = 0 \quad (6b)$$

where \mathbf{t}_k is the tangential unit vector. Since velocity continuity across the interface is assumed (a low Mach number assumption) then the energy jump condition of Eq. (3c) can be readily simplified by subtracting $\mathbf{u}_k \cdot (\text{Eq. (3d)})/2$ from it to remove the mechanical energy (it does not matter if \mathbf{u}_k is that of the gas or solid since they are assumed to be the same at the interface) resulting in,

$$[[\sum_i (e_{k,i} \dot{m}_{k,i}'' - \dot{q}_k'')]] = \sum_i [[e_{k,i} \dot{m}_{k,i}'']] - [[\dot{q}_k'']] \quad (7)$$

where $\dot{m}_{k,i}'' (= Y_k \dot{m}_k'' + \dot{m}_i''^{diff})$ is the mass flux of the i th species in the k th material across the interface. For charring materials, a detailed model of the movement of pyrolysis gases within the solid is used and the interface is treated as a blowing surface. Under these circumstances, $[[\dot{m}_{k,i}'']] = [[\dot{m}_k'' Y_{g,i} - \mu \nabla Y_i / Sc]] = 0$, which could be used to define a reflection condition for $Y_{g,i}$ by either knowing the mass flux at the interface or the species mass fractions in the solid porous material. However, it was found to be difficult to ensure mass conservation across the interface at low mesh resolutions and the resulting simulation often became unstable. Alternatively, the integrated mass flux across the interface is used to deposit the exchange of mass, momentum and energy from surface blowing into the Eulerian field using a source deposition procedure (to be discussed in Section 3.2.1) which ensures conservation principles are strictly enforced resulting in a robust coupling algorithm. For this case, the role of the ghost–fluid mirroring is to enforce a zero penetration of the species mass flux,

$$\nabla Y_{g,i} \cdot \mathbf{n}_g = 0 \quad (8)$$

since the actual mass transfer is already accounted for using the source term deposition procedure. In the numerical implementation, however, this condition is not precisely satisfied. The reason is the discrepancy between the interpolants used to populate the ghost–fluid and that used to calculate species flux near the fluid–solid interface. A simple fix for eliminating the mass leakage is given in Section 3.2.1.

For non-charring materials, the pyrolysis process is treated as a surface phenomena and the effects of surface blowing are treated in a similar fashion with the Lagrangian model providing the total amount of mass, momentum and energy over a given coupling interval. In this case, Eq. (7) is used to determine the surface pyrolysis rate per unit area, $\dot{m}_{pyr}'' = (e_g + \Delta h_{pyr})/(\dot{q}_g'' + \dot{q}_s'')$ where Δh_{pyr} is the heat of pyrolysis.

Since a separate source term deposition approach is used for both the charring and non-charring materials then the effects of surface blowing may be ignored in Eq. (7) resulting in the following jump conditions that are used to specify the gas-phase temperature in the ghost–fluid,

$$[[\dot{q}_k'']] = [[k_k \partial T / \partial n_k]] = 0. \quad (9)$$

For adiabatic walls, $\dot{q}_s'' = 0$, therefore the condition for the ghost–fluid specification is $\partial T_g / \partial n_g = 0$. For non-adiabatic walls, the temperature at the interface is specified by the Lagrangian model and the gas-phase temperature is extrapolated into the ghost–fluid.

2.2. Lagrangian model of charring solid

The modeling of thermal and gas transport within the structures is based on a homogenization theory developed for examining the thermal and mechanical response of charring polymer composites [13,14,16]. Individual gaseous species are tracked through the phase averaged species mass conservation equations. The total number of gaseous species depends upon the complexity of the pyrolysis model and must equal the gas species in the Eulerian model. Phase-averaged species conservation equations are solved for the bulk density, ρ_g , and the mass fraction of the i th gas constituent, $Y_{i,g}$,

$$\partial(\phi_g \rho_g)/\partial t = \nabla \cdot (\rho_g \mathbf{K}_{\sim} \cdot \nabla p_g / \mu_g) + \dot{m}_{i,int}''' \quad (10a)$$

$$\partial(\phi_g \rho_g Y_{i,g})/\partial t = \nabla \cdot (\rho_g Y_{i,g} \mathbf{K}_{\sim} \cdot \nabla p_g / \mu_g) + \nabla \cdot [\rho_g \phi_g D_{i,m} \nabla Y_{i,g}] + \dot{m}_{k,vol}''' \phi_g + \dot{m}_{i,int}''' \quad (10b)$$

where Darcy's Law is employed to approximate the bulk gas transport, i.e., $\phi_g \mathbf{u}_g = -\mathbf{K} \cdot \nabla p_g / \mu_g$ requiring the specification of the permeability, \mathbf{K} . Fick's Law of diffusion is used to account for effects of differential diffusion, i.e., $\mathbf{u}_{i,diff} = -(D_{i,m} \nabla Y_{i,g}) / Y_{i,g}$ where $D_{i,m}$ is the effective binary diffusion coefficient for the i th species in the mixture. The third term on the RHS of Eq. (10b) accounts for production or consumption of species from volumetric reactions within the gas phase (e.g., oxidation of pyrolysis gases within the material) and the last term accounts for the production of pyrolysis gases from endothermic decomposition and evaporation processes which occur at phase interfaces. For the solid phases, the species conservation equation simplifies since the density is assumed to be constant, i.e., $\rho_{i,s} \partial \phi_{i,s} / \partial t = \dot{m}_{i,int}'''$. Thermal equilibrium among the solid and gas phases is assumed resulting in a single equation to describe energy transport,

$$\begin{aligned} \rho C_p \partial T / \partial t = & \nabla T \cdot [\rho_g C_{p,g} \mathbf{K}_{\sim} \cdot \nabla p_g / \mu_g] + \nabla \cdot (\mathbf{K} \cdot \nabla T) + \sum_{k=1}^{N_g} (\nabla T \cdot C_{p,k} \rho_g \phi_g D_{k,m} \nabla Y_{k,g}) - \sum_{k=1}^N h_k (\phi_g \dot{m}_{k,vol}''' + \dot{m}_{k,int}''') \\ & + \partial(\phi_g p_g) / \partial t - \nabla \cdot (p_g \mathbf{K}_{\sim} \cdot \nabla p_g / \mu_g) \end{aligned} \quad (11)$$

where $\rho (= \sum \rho_i \phi_i)$ and $C_p (= \sum \phi_i \rho_i / \rho C_{p,i})$ are the bulk density and specific heat, respectively. The terms on the RHS of Eq. (11) represent bulk advection (via the Darcy's Law approximation), conduction, differential diffusion, oxidation/decomposition rate processes and the material derivative of pressure.

For ignition and flame spread studies, the swelling of the laminate from char formation can have a pronounced effect on ignition times and flame spread rate. To account for these effects, an evolution equation for the i th solid volume fraction can, in principle, be derived,

$$\frac{D\phi_i}{Dt} = \frac{\dot{m}_{i,int}'''}{\rho_i} + \dot{V}_{i,exp} \quad (12)$$

where the subscript $i (= f, r, c)$ represents either fiber, resin or char with an associated density, ρ_i (mass of i th constituent per unit volume of the i th constituent), and corresponding source/sink term, $\dot{m}_{i,int}'''$, from pyrolysis reactions. The second term on the RHS of Eq. (12) accounts for the increasing solid volume fraction from swelling (expansion) processes and can be directly related to the divergence of the i th solid material velocity, i.e., $\dot{V}_{i,exp} = -\phi_i \nabla \cdot \mathbf{u}_i$. To rigorously account for the effects of swelling requires a detailed analysis of the mechanical response of the structure to determine \mathbf{u}_i that, in turn, will depend on the thermal field (via, thermal expansion, fiber fraying, etc.). To model this coupled thermo-mechanical system, a presumed micro-mechanics description is often defined in the context of unit cell homogenization approaches [14]. The exact nature of the swelling process is, however, quite complicated and potentially difficult to validate experimentally. A simpler phenomenological approach is therefore pursued where the solid volume fraction is directly expressed as a linear function of a reaction progress variable describing the extent of pyrolysis (α),

$$\phi_i = \phi_{i,o} + (\phi_{i,f} - \phi_{i,o})\alpha \quad (13)$$

where the initial ($\phi_{i,o}$) and final ($\phi_{i,f}$) volume fractions of each solid constituent. Table 1 summarizes these values for the carbon-epoxy laminate system of this study.

This simple model accounts for the leading order effects from composite swelling which is to decrease the solid volume fractions and increase the gas volume fraction. In addition, the composite geometry change from swelling is also accounted for using a newly developed element expansion algorithm [17]. In this approach, each element node located at position \mathbf{x}_o is first assigned a neighboring reference node, $\mathbf{x}_{o,ref}$. The distance between these nodes at the start of the simulation is defined as: $\mathbf{d}_o = \mathbf{x}_o - \mathbf{x}_{o,ref}$, as shown in Fig. 1. As the expansion process proceeds the distance between the two nodes is directly related to the expected volumetric expansion, V/V_o , via, $\mathbf{d} = \mathbf{d}_o V/V_o$, where V/V_o can be determined [17],

$$\frac{V}{V_o} = \frac{(\rho_e V_e / V_o - \rho_o)\alpha + \rho_o}{\rho} \quad (14)$$

resulting in a non-linear dependence of V/V_o on α . Additional details on the swelling model can be found in Ref. [17].

3. Numerical formulation

The overall computational approach is based on the coupling of Computational Fluid Dynamics (CFD) with FE representations of solids. The flow field modeling is based on the use of Large Eddy Simulation (LES) developed for examining buoyancy driven plumes [18] and pool fires [19,20]. A summary of the numerics used in the finite volume formulation of the LES and FE formulation of the structure are given in Sections 3.4 and 3.5, respectively.

In the following subsections, the treatment of the fluid–solid interface is described using a level set description that makes use of an efficient re-initialization procedure to update the level set for moving interfaces. Next, the ghost–fluid update is described in Section 3.2 using a reflection and interpolation procedure with details of the surface blowing in Section 3.2.1.

3.1. Efficient level set initialization and update

The fluid–solid interface is defined as the zeroth level of a level set function, γ_k , a signed distance function defined as, $\gamma_k(\mathbf{x}, t) < 0$ when \mathbf{x}_k lies in the k th material region and for which the surface normal and curvature are defined as, $\mathbf{n}_k = \nabla\gamma_k$ and $K_k = -\nabla^2\gamma_k$, respectively. One of the advantages of using a level set function to describe the interface is the ease of computing wall normal heat flux to the solid from the gas, $\dot{q}_g'' = -k_g \nabla T_g \cdot \mathbf{n}_g = -k_g \nabla T_g \cdot \nabla\gamma_g$ where simple central differencing may be used to approximate ∇T and $\nabla\gamma_g$ since both T and γ_g are continuous across the interface.

For moving interfaces, additional computational cost is introduced for the re-initialization of the level set function on the Eulerian mesh at each coupling interval. Efficient numerical algorithms to re-initialize the level set include: the fast marching methods [21], pseudo-time relaxation procedures [22] and method of characteristics [23]. All of these methods have an predefined error tolerance that is set to result in accurate estimates of the level set function near the fluid–solid interface and coarser estimates for locations far from the interface.

In this study, a new methodology is developed that results in the exact value of the level set function near the interface without iteration and is suitable for execution on parallel computers. A triangulated surface mesh is first extracted from the surface of the FE model and sent to each region of the CFD over all processors. Since the surface mesh typically has a low memory footprint, repeated storage of it over all processors doesn't present a problem. The surface mesh serves as the basis for defining the interface for each CFD block region. The accuracy of the re-initialization is therefore as accurate as the triangulated surface mesh representation of the geometry. A normalized level set measure is introduced to define regions of the flow from near to far from the fluid–solid interface to allow a balance of accuracy and computational cost, $\gamma^* (= \gamma_g/\gamma_{g,max})$, with $\gamma_{g,max}$ being a characteristic size of the computational domain. The location $\gamma_o^* \equiv C\Delta x_{max}/\gamma_{g,max}$ defines the value of γ^* that separates the near-field from the far-field where Δx_{max} is the largest grid cell and C is a proportionality constant that is set to the maximum interpolant stencil size.

For values of $\gamma^* \leq \gamma_o^*$, the CFD node of interest, \mathbf{x}_p , is in the near-field and the level set (γ_g) is initialized using the triangulated surface mesh. Two categories of nodes are defined for this operation and are classified as either “inside” or “outside” the projected volume of a surface element shown in Fig. 2 for a 2D surface. The projected volume is defined as the volume created by sweeping the element surface area of the triangle along its normal direction. Using this classification, points 1, 3, and 4 are deemed as inside nodes while node 2 is an outside node. Note, this classification has no relation to if the nodes lie in the gas or solid phases – as shown in Fig. 2 nodes 1 and 3 are in one phase and node 4 in the other, yet they are all classified as inside nodes. For these nodes, the shortest distance is the surface normal distance (\bar{d}_{p1} , \bar{d}_{p3} and \bar{d}_{p4}). Node 2 in Fig. 2, however, does not lie within the projected volume of any of the elements and therefore is classified as an outside node. For this node, the shortest distance ($d_{p,2}$) is the closet node on the surface mesh.

The algorithm for sorting CFD nodes and determining γ_g begins with a nodal search to determine the closest surface node, \mathbf{x}_c , to the CFD node, \mathbf{x}_p , as shown in Fig. Fig. 3. The purpose of this search is to quickly reduce the number surface elements considered for determining the shortest distance to the surface. A collection of candidate elements are then defined which are the elements that share \mathbf{x}_c in common, as identified with dashed lines in Fig. 3 (4 in total). A connectivity list relating nodes to candidate elements is pre-computed at the beginning of the simulation and stored and used thereafter, therefore the search for candidate elements only occurs once. Next, an estimate of the shortest distance, $|\mathbf{d}_e|$, from \mathbf{x}_p to the surface is computed for each element. The evaluation of $|\mathbf{d}_e|$ for each candidate element differs depending on whether \mathbf{x}_p is either inside or outside the projected area of element e . The classification is established based on the element surface normal (\mathbf{n}_e) and the surface normals ($\mathbf{n}_1, \mathbf{n}_2, \mathbf{n}_3$), shown in Fig. 3, and are defined as:

Table 1
Summary of the initial and final volume fractions of the fiber (f), resin (r), gas (g) and char (c) constituents.

| i | $\phi_{i,o}$ | $\phi_{i,f}$ |
|-----|--------------|--------------|
| f | 0.600 | 0.273 |
| r | 0.393 | 0.000 |
| g | 0.007 | 0.706 |
| c | 0.000 | 0.021 |

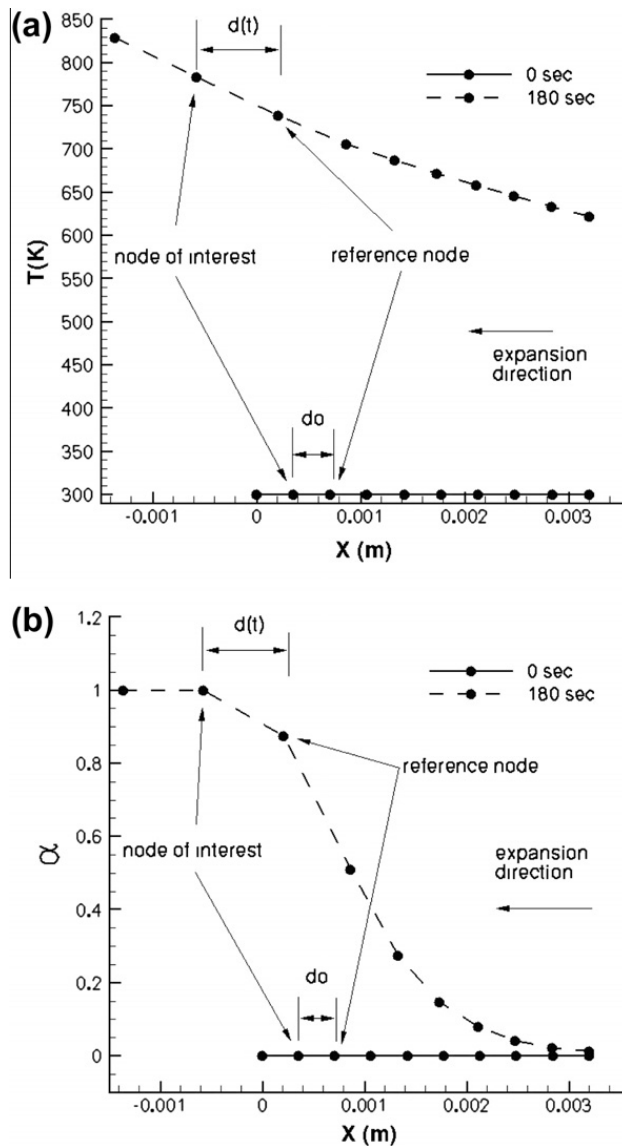


Fig. 1. Element expansion process in 1D for (a) temperature and (b) reaction progress variable at $t = 0$ s and 180 s.

$$\mathbf{n}_e = \mathbf{x}_{1 \rightarrow 2} \times \mathbf{x}_{1 \rightarrow 3} \quad (15a)$$

$$\mathbf{n}_1 = \mathbf{x}_{2 \rightarrow 3} \times \mathbf{n}_e \quad (15b)$$

$$\mathbf{n}_2 = \mathbf{x}_{3 \rightarrow 1} \times \mathbf{n}_e \quad (15c)$$

$$\mathbf{n}_3 = \mathbf{x}_{1 \rightarrow 2} \times \mathbf{n}_e \quad (15d)$$

where $\mathbf{x}_{i \rightarrow j} \equiv \mathbf{x}_j - \mathbf{x}_i$. If the result of projecting all vectors from \mathbf{x}_p to the element vertexes onto the surface normal of the corresponding side are negative, $[(\mathbf{x}_{1 \rightarrow p} \cdot \mathbf{n}_3 \leq 0), (\mathbf{x}_{2 \rightarrow p} \cdot \mathbf{n}_1 \leq 0), (\mathbf{x}_{3 \rightarrow p} \cdot \mathbf{n}_2 \leq 0)]$, then the point is deemed inside the projected element volume and the magnitude of the normal distance vector between \mathbf{x}_p and the element plane is defined as: $|\mathbf{d}_e| = \mathbf{n}_e \cdot \mathbf{x}_c$. If the point is not inside then it must lie outside of the projected volume. In this case, the shortest distance is defined as the minimum distance from \mathbf{x}_p to each of the nodes comprising the element. The final value of the shortest distance from the surface to node \mathbf{x}_p (in magnitude) is taken as the minimum value over all candidate elements, i.e., value of $|\mathbf{d}| = \min_{e=1}^N (|\mathbf{d}_e|)$. The direction of \mathbf{d} is taken as that of the area normal of the element with the minimum value of $|\mathbf{d}_e|$. The value of γ_g is then set equal to $\gamma_g = |\mathbf{d}| \frac{(\mathbf{x}_{p \rightarrow c} \cdot \mathbf{n}_e)}{|\mathbf{x}_{p \rightarrow c} \cdot \mathbf{n}_e|}$, where $(\mathbf{x}_{p \rightarrow c} \cdot \mathbf{n}_e)$ will be negative for CFD nodes within the fluid and positive for values in the ghost-fluid nodes.

For \mathbf{x}_p nodes that are classified as outside, more than one element will always be selected since \mathbf{x}_c is shared by more than one element. To uniquely identify the candidate element that is closer, the sides of each triangular element are shifted

slightly inward along the normal by a tiny constant (1×10^{-10} m) thereby separating each element and producing unique results.

If $\gamma^* > \gamma_o^*$ then \mathbf{x}_p is in the far-field and only a crude, inexpensive, estimate of the signed distance is required. In the far-field, the signed distance is not used directly in the ghost-fluid method, rather it only serves as an indicator for when more refined estimates are needed. To reduce computational cost, a sequence of “patches” are constructed from the original surface mesh as illustrated in Fig. 4 and associated (negative) patch levels are defined as:

$$l = \text{int}[l_{\min}(\gamma^* - \gamma_o^*) / (1 - \gamma_o^*)] \tag{16}$$

which satisfies the limits that as $\gamma_g \rightarrow \gamma_{\max}$ then $\gamma^* \rightarrow 1$ and $l \rightarrow l_{\min} < 0$. The appeal of the patches is to reduce the number of distance calculations required to estimate the distance function by using the patch topology rather than the elements. Starting from a patch level of zero (the baseline surface mesh) decreasing levels are constructed using a grouping algorithm of the triangles first and then of the patches at lower patch levels. A starting node is first identified to construct patches at level -1 and is (arbitrarily) chosen to be the first node in the data array defining the unstructured list of nodes defining the surface mesh. This starting node defines the origin of the first patch at level -1 . This first patch is the collection of surface nodes connected to the starting node through surface elements as shown in red in Fig. 4. The origin of the next patch at level -1 is the next node in the surface mesh data array that has not been used in patch 1 and an associated patch is defined for it (patch 2). This process is repeated until all of the surface nodes are grouped into patches at level -1 . Patch connectivity at level -1 is established if two or more patches share the same surface mesh node. The connectivity list is used to group patches at level -1 to form super patches at level -2 , as shown in Fig. 4. The origin of patch 1 at level -2 is set equal to that of the first patch at level -1 . The origin of the next super patch at level -2 (patch 2) is defined using the next available patch at level -1 from the list of all patches at level -1 that has not been already used in patch 1. The grouping of patches continues and associated (negative) levels are defined until a single super patch is created that contains all of the surface nodes. Fig. 4 illustrates this progression up to a patch level of -4 .

Since the patches do not retain surface normal information, the sign of γ_g cannot be readily deduced – only its magnitude. To determine the sign of γ_g , the near-field algorithm is used only once at the beginning of the simulation and stored for all nodes. Subsequent far-field evaluations using patches then update the magnitude of γ_g until the interface becomes sufficiently close where the near-field algorithm is employed. The evaluation of the local level using the linear interpolation given by Eq. (16) uses γ_g^* from the previous coupling time step. This provides a continuous degradation in the estimate of γ_g but with an associated savings in computational cost. While more sophisticated far-field level indicators could be devised, the linear degradation model is found to be satisfactory for all of the problems considered in this study.

To illustrate the use of patches, Fig. 5 shows the use of patches for a simple 2D problem for which the surface mesh is represented by a collection of lines. To the left of each diagram is the solid represented by a surface mesh. To the right is an Eulerian mesh used by the CFD. The original surface mesh using patches are shown in Fig. 5(a), (b), (c) and (d) for patch levels of -1 , -2 and -3 , respectively. Each patch is represented by a different colored line, e.g., five patches are shown at level -2 in Fig. 5(c). Plotted on the right of each surface mesh are contours of the level set function γ_g using the original surface mesh (Fig. 5(a)) and then using progressive coarsening of it using patches. It should be emphasized that the initialization of γ_g near the surface is intentionally poor to illustrate the use of patches. In practice, near the surface $\gamma^* < \gamma_o^*$ and therefore the use of patches is not appropriate and the near-field algorithm would be used instead to provide the exact value of γ_g .

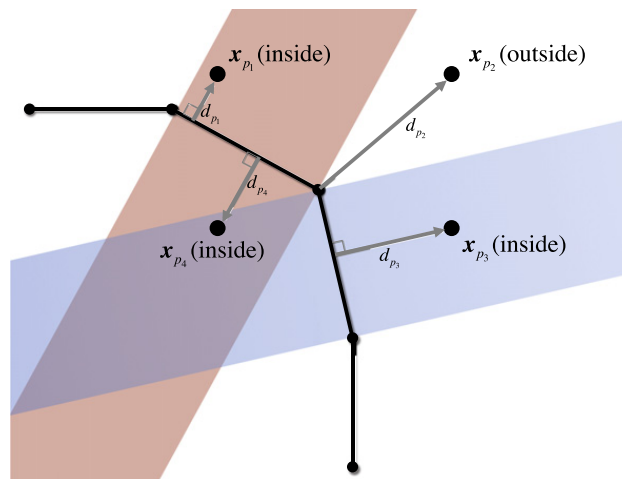


Fig. 2. Classification of CFD nodes as either being defined as either inside ($\mathbf{x}_{p1}, \mathbf{x}_{p3}, \mathbf{x}_{p4}$) or outside (\mathbf{x}_{p2}) the projected volumes associated with the surface mesh.

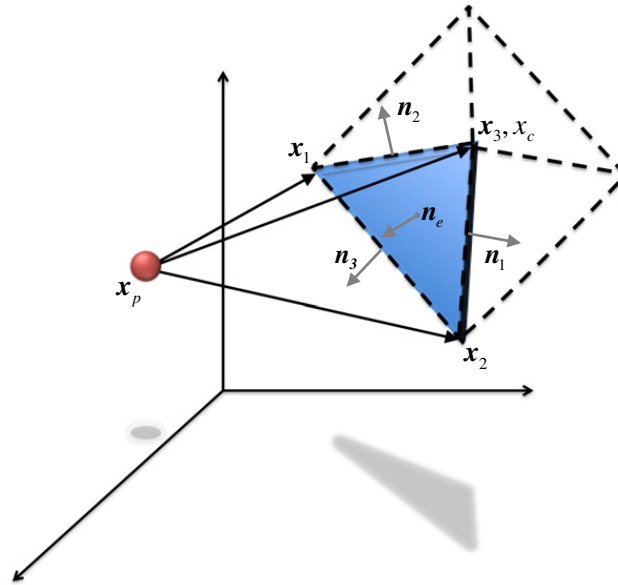


Fig. 3. Identification of nearest node (x_c) and attached surface elements for the calculation of the of level set function.

3.2. Ghost–fluid implementation

The update of the Eulerian solver near the immersed interface is accomplished using a ghost–fluid methodology. In this approach, a relatively narrow range of ghost–fluid cells are defined near the boundary of the fluid–solid interface. The means of populating the properties of the ghost–fluid cells and interface description distinguishes one embedded methodology from another. Several variants of ghost–fluid cell updates have been tailored for the use of level set interface descriptions for both incompressible [8] and compressible [24–27,5] flows and are problem dependent. In the original ghost–fluid method for Eulerian–Eulerian multi-material descriptions, continuous variables (e.g., pressure and velocity) from one material populate the ghost-cells of a neighboring material while discontinuous variables (e.g., entropy) are extrapolated [26]. For the Eulerian–Lagrangian extension of the ghost–fluid method, the ghost-cell pressure is determined from the Eulerian field through extrapolation (i.e., $[p] = 0$) and velocity extrapolated from the Lagrangian field to the ghost-cells (i.e., $[u_n] = 0$). Recently Sambasivan and UdayKumar have summarized the more popular methods to update the ghost-cells using (1) a simple reflection, (2) a local Riemann solver, and (3) method of characteristics [15]. In their study, they show the issues of over/under heating errors from shock impact on solids using a simple reflection methodology for which several fixes have been proposed in the literature (e.g., Fedkiw’s isobaric fix [8]). For the current low Mach study, these errors do not arise even though a fully compressible flow formulation is employed therefore only a simple reflection strategy is required.

The linear mirroring extrapolation of Ye et al. [28] is employed that has been used in ghost–fluid studies of both incompressible [2] and compressible [27,15] flows. In this approach, linear extrapolation to the ghost region is achieved by first computing the location of the mirror image of a given ghost node, \mathbf{x} , that is defined along the line normal to the interface at a location that is equidistant (γ_g) from the interface in the (solved) Eulerian gas field, as shown in Fig. 6,

$$\mathbf{x} = \mathbf{x}_G + 2\gamma_g(\mathbf{x}_G)\mathbf{n}_g \tag{17}$$

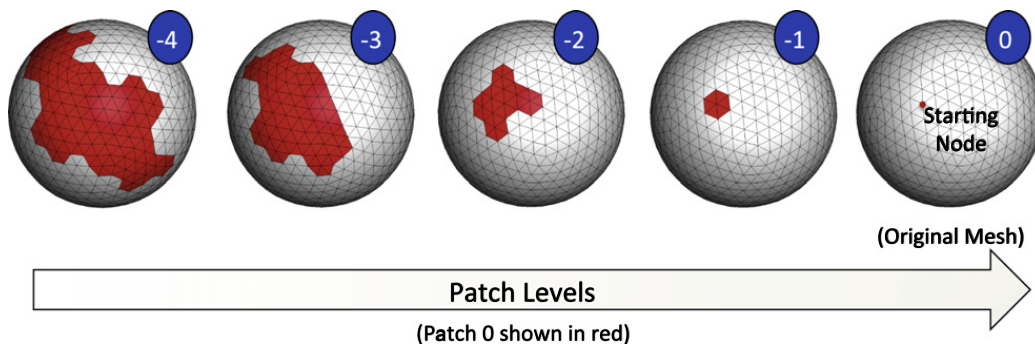


Fig. 4. Illustrations of patch level growth starting from the original surface mesh.

where \mathbf{x}_G is the location of the ghost node of interest. Once \mathbf{x} is identified, then a local stencil can be defined in the vicinity of that location for a Newton interpolating polynomial. Using the interpolating polynomial, the interface constraints summarized in Eqs. (5),(6),(8) and (9) are imposed at the intersection between the line connecting points \mathbf{x}_G and \mathbf{x} and the fluid–solid interface. The result is a local 4×4 matrix in 2D or a 8×8 matrix in 3D that must be inverted to solve for the unknown scalar value at \mathbf{x}_G . Additional details on this approach can be found in Refs. [28,15]. For a fixed mesh, the matrix inversion is pre-computed *a priori* for each ghost node and associated interpolation weights are stored for either a Neumann type (e.g., pressure in Eq. (5)) or Dirichlet type (e.g., velocity in Eq. (6)) boundary to avoid unnecessary repetitive matrix inversions. The weights are then recomputed every time the Lagrangian mesh is moved.

3.2.1. Mass transfer implementation

As discussed in Section 2, the effects of surface blowing from off-gassing are superimposed through an explicit source term deposition into the Eulerian gas field. To avoid double counting, the implicit mass flux through the fluid–solid interface must therefore be identically equal to zero. While the errors using a standard ghost–fluid method are sufficiently low for capturing solid boundaries, it is not sufficiently accurate for problems involving ablation or surface blowing since the numerical errors are large relative to the flux of mass, momentum and energy. The error is especially pronounced for flame spread problems. A relatively low flux error in mass flux will create an imbalance of chemical energy to the gas phase that will falsify the flame spread rate. One way to reduce the mass leakage is to either use higher-order approximations to the linear mirroring or use a finer mesh in the vicinity of the fluid–solid interface. Both of these solutions result in additional computational expense. A simpler solution is used in this study where the mass flux through cell faces containing the fluid–solid interface are simply set equal to zero by setting the associated area of that surface to zero in the context of the finite volume solution. The advantage of this mass transfer approach is to ensure that overall mass (ΔM_i and ΔM), momentum ($\Delta \mathbf{U}$) and energy (ΔE) exchanged across the interface is exactly preserved. In this approach, the mass, momentum and energy to be transferred to the gas field is integrated over the surface of the solid Lagrangian model, Γ_s , and over a defined coupling time, Δt_c , (to be defined in Section 3.3),

$$\Delta M_i^e = \int_t^{t+\Delta t_c} \int_{\Gamma^e} \dot{m}_i' d\Gamma^e dt \tag{18a}$$

$$\Delta M^e = \sum_i M_i^e \tag{18b}$$

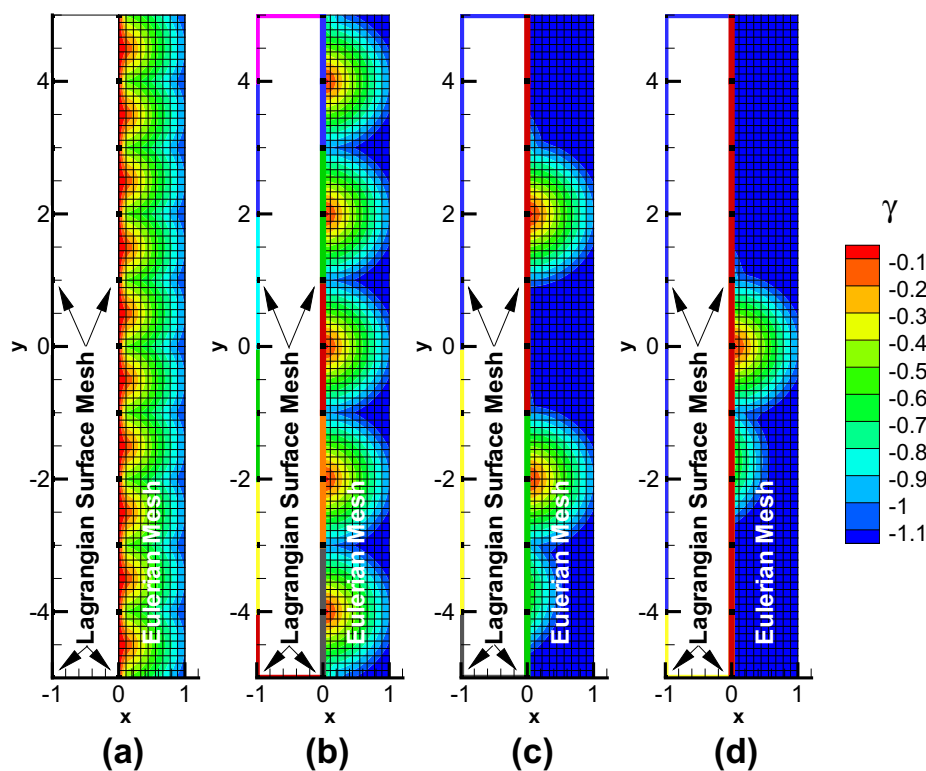


Fig. 5. Level set function initialization with patch levels of (a) 0 (original mesh), (b) -1 , (c) -2 and (d) -3 for every node n in the Eulerian mesh. Patches are indicated as different colored lines on the surface mesh (a rectangle).

$$\Delta \mathbf{U}^e = \int_t^{t+\Delta t_c} \int_{\Gamma^e} \dot{m}_i'' \mathbf{u}_s d\Gamma^e dt \tag{18c}$$

$$\Delta E^e = \int_t^{t+\Delta t_c} \int_{\Gamma^e} \dot{m}_i'' \left(e_g + \frac{1}{2} \|\mathbf{u}_s\| \right) d\Gamma^e dt \tag{18d}$$

where superscript e represents an element with surface Γ^e that lies on $\partial\Omega_s$ so that $\partial\Omega = \sum_e \Gamma^e$. The source term for each element is distributed in the gas field centered about \mathbf{x}^e which is defined as the element face centroid, $\mathbf{x}^e = (\sum_i \mathbf{x}_i^\Gamma) / N^\Gamma$, where \mathbf{x}_i^Γ is the position of the element face vertices and N^Γ is the total number of vertices on the element face. The element face source term, $S^e = \{\Delta M_i^e, \Delta M^e, \Delta \mathbf{U}^e, \Delta E^e\}$, is distributed in the flow field about \mathbf{x}^e evenly amongst deposition nodes \mathbf{x}_j . The deposition nodes are selected adjacent to the element face covering the approximate area of the element. This is accomplished by tagging the first node along the outward surface normal that is in the gas phase ($\gamma_g < 0$). A sphere is then defined, centered about \mathbf{x}^e , with a radius that results in an area equal to Γ^e when a slice is taken through the center of the sphere. In three dimensions these assumptions results in a radius of $r^e \approx (\Gamma^e/\pi)^{1/2}$. If there are no tagged nodes within the sphere the radius is repeatedly increased until at least one node is identified. The source term weights are pre-computed and stored to minimize computational cost of multiple source term use. The weights are only re-initialized when the Lagrangian mesh moves.

3.2.2. Heat flux implementation

The heat flux (\dot{q}'') from the CFD is computed in terms of the normal temperature gradient which is expressed in terms of gradients in the temperature and level set function,

$$\dot{q}'' = -k_g \partial T / \partial n_g = -k_g \nabla T \cdot \nabla \phi_g \tag{19}$$

where n_g is outward surface normal direction from the gas phase. The gradients are computed using high-order Lagrangian interpolating polynomials which are constructed from CFD nodes in the vicinity of the point of interest where the heat flux is required. In this approach, the scalar variables are represented using either 2D or 3D basis functions (ψ). For example, the temperature in 2D may be expressed as,

$$T(\mathbf{x}, t) = \sum_i \sum_j \psi_{ij}(\zeta(\mathbf{x})) T_{ij}(t) \tag{20}$$

where \mathbf{x} is the point of interest to evaluate the heat flux and ζ is the associated curvi-linear coordinate in the body fitted coordinate system for the CFD mesh. The subscript (i, j) corresponds to the location in a 2×2 matrix of nodes defining the extent of the interpolant. The basis functions are expressed as the product of 1D basis functions in each of the respective curvi-linear directions,

$$\psi_{ij} = \psi_i^{1D}(\zeta_1) \psi_j^{1D}(\zeta_2) \tag{21}$$

where $\psi_i^{1D}(\zeta_1)$ and $\psi_j^{1D}(\zeta_2)$ are the associated basis function for the first and second curvilinear directions that are expressed in terms of generalized Lagrange interpolating polynomials of order N ,

$$\psi_i^{1D}(\zeta_1) = \prod_{p=0, p \neq i}^{N+1} \frac{\zeta_1 - \zeta_p}{\zeta_i - \zeta_p} \tag{22a}$$

$$\psi_j^{1D}(\zeta_2) = \prod_{p=0, p \neq j}^{N+1} \frac{\zeta_2 - \zeta_p}{\zeta_j - \zeta_p} \tag{22b}$$

Using Eq. (20), the gradient of temperature can be determined analytically and expressed in terms of derivatives of the basis functions from the curvilinear coordinate system,

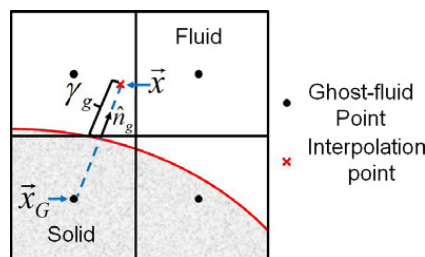


Fig. 6. Ghost–fluid mirroring showing the ghost–fluid node of interest, \mathbf{x}_G and its evaluation using linear extrapolation across the interface from the gas-phase at location, \mathbf{x} .

$$\nabla T = \mathbf{g}^k \partial T / \partial \zeta_k = \mathbf{g}^1 \sum_i \sum_j T_{ij}(t) \frac{\partial \psi_i^{1D}}{\partial \zeta_1} \psi_j^{1D} + \mathbf{g}^2 \sum_i \sum_j T_{ij}(t) \frac{\partial \psi_j^{1D}}{\partial \zeta_2} \psi_i^{1D} \quad (23)$$

where $\mathbf{g}^k (\equiv \hat{e}_j \partial \zeta_k / \partial x_j)$ is the contra-variant vector [29] that is evaluated locally using the same set of basis function as that used for the temperature. The derivatives of ψ_i^{1D} and ψ_j^{1D} in Eq. (23) can be determined analytically resulting in the following result.

$$\frac{\partial \psi_i^{1D}}{\partial \zeta_1} = \sum_{p=0, p \neq i}^{N+1} \frac{1}{\zeta_i - \zeta_p} \prod_{q=0, q \neq i}^{N+1} \frac{\zeta_1 - \zeta_q}{\zeta_i - \zeta_q} \quad (24a)$$

$$\frac{\partial \psi_j^{1D}}{\partial \zeta_2} = \sum_{p=0, p \neq j}^{N+1} \frac{1}{\zeta_j - \zeta_p} \prod_{q=0, q \neq j}^{N+1} \frac{\zeta_2 - \zeta_q}{\zeta_j - \zeta_q}. \quad (24b)$$

For the present study, second-order polynomials are used (i.e., $N = 2$) resulting in 3×3 node stencil in 2D or $3 \times 3 \times 3$ node stencil in 3D for the construction of the heat flux. The stencil nodes are selected such that all of the nodes are located within the fluid. Once the nodes are selected then the gradients may be determined using Eqs. (23) and (24). In practice, the computed weights (e.g., $\psi_j^{1D} \partial \psi_i^{1D} / \partial \zeta_1$) that multiply T_{ij} are precomputed and stored for later use each time the interface moves to minimize computational cost of repetitive calculations when computing gradient quantities at the interface.

3.3. Coupling time interval

If the source terms from surface blowing, discussed in Section 3.2.1, are directly deposited over a single CFD time step (Δt_{CFD}) then an artificially small time step is required to maintain numerical stability. To mitigate this potential problem, a dynamic time stepping algorithm is developed for coupling along with a robust mechanism to integrate the source terms into the gas phase solution. In this approach, a future coupling time step, Δt_c^{n+1} is estimated using a current estimate of the coupling time step, Δt_c^n , and the previous coupling time step, Δt_c^{n-1} , using a time relaxation relation, $\Delta t_c^{n+1} = \Delta t_c^{n-1} + \omega_r (\Delta t_c^n - \Delta t_c^{n-1})$, where ω_r is a relaxation factor and set equal to a value of 0.1. The value of Δt_c^n is the minimum coupling time scales for mass ($\Delta t_{c,mass}$), momentum ($\Delta t_{c,mom}$) and energy ($\Delta t_{c,ener}$) exchange over all Eulerian nodes that are affected by the source term deposition, and are computed as follows.

$$\Delta t_{c,mass} = F_{mass} (\rho_g V_g) / \Delta M_j^e \quad (25a)$$

$$\Delta t_{c,mom} = F_{mom} \text{MIN} \left[(\rho_g u_k V_g) / \Delta U_{j,k}^e \right] \quad (25b)$$

$$\Delta t_{c,ener} = F_{ener} (\rho_g E_g V_g) / \Delta E_j^e \quad (25c)$$

where F_{mass} , F_{mom} and F_{ener} are safety factors that are all set equal to 0.1. The source terms that are passed from the Lagrangian model to the Eulerian field are integrated into the gas-field solution over a time, Δt_c^{n+1} , by distributing the total source terms over the time remaining until the next coupling time, $t_c = t + \Delta t_c^{n+1}$. In this approach, the total source of mass, momentum and energy from surface blowing for a given Eulerian node is first determined by summing over all elements at the start of a coupling interval, i.e., $S_{ij,k} = \sum_e S_{ij,k}^e$. During the coupling time interval the total source is decremented a factor $\Delta S_{ij,k} = S_{ij,k}(t_c - t) / \Delta t_{CFD}$ and $\Delta S_{ij,k}$ is treated as a constant source during that CFD time step. The process is repeated over each CFD time step until the residual source is driven to zero at time t_c .

3.4. CFD numerics

The flow solver used is based on a finite volume formulation using the AUSM family of flux splitting schemes [30,31] using a low Mach number preconditioning for efficient integration at low speeds [18]. Fluxes at the cell faces are interpolated using upwind biased stencils [32] for momentum and essentially non-oscillatory polynomials (ENO) [33] for density, energy and reacting species. The equations are integrated in time using a second order Runge–Kutta with standard weights. A block-structured domain decomposition is employed to partition the solution integration over multiple processors. A region communicates with neighboring blocks through a ghost cell (not to be confused with ghost–fluid cells) strategy using a native Java version of the message passing interface (MPI) [34].

3.5. FE numerics

Eqs. (10) and (11) are solved using a Galerkin finite element formulation using high-order Lagrange interpolating polynomials for hexahedral elements. The FE domain is decomposed for solution on parallel computing platforms using a Lagrange multiplier decomposition [35] with a customized global bi-conjugate gradient solver [36] to solve for the reduced system over multiple processors. Fig. 7 shows representative results using this approach for modeling the decomposition

of glass/ phenolic composite material at three locations in the material. Symbols are experimental data and solid lines are predictions using current thermal mechanical damage model (TMDM). For this material the solid phases consist of resin, fiber, and char. As shown in Fig. 7(a) temperature predictions are in excellent agreement with the data, however, differences are observed in the predictions of internal gas pressure, as shown in Fig. 7(b), due to the challenges in obtaining reliable models of permeability for charring materials.

4. Results

In the following subsections several benchmark problems are first explored to assess the accuracy of the algorithm. The first three benchmark problems explore the errors associated with moving interfaces, flow over a cylinder and heat transfer from an isothermal plate.

4.1. Conservation error checks

It is well known that ghost–fluid methods are not conservative [26,4]. In order to determine the conservation errors associated with the immersed boundary method used in this study, a sinusoidally translating cylinder (2D) and sphere (3D) with isothermal solid wall boundary conditions at the domain edges is examined. The total mass should stay constant throughout the problem. For all cases the diameter of the sphere and cylinder is 1.6 cm, and the domain is 10 cm × 3 cm in 2D and 10 cm × 3 cm × 3 cm in 3D. For all cases the object is moved periodically from $x = 0$ to 8 cm with a period of 5 ms, which represents an average velocity of 32 m/s. For both objects low and high resolution cases are examined, corresponding to a mesh spacing of 1 mm and 0.25 mm, respectively. For all cases the object boundary condition is adiabatic with no-slip and the domain is initialized with air at standard atmospheric conditions.

Fig. 8(a) and (b) show the vorticity at a time of 2.55 s. The resulting complex flow field shows that the ghost–fluid immersed boundary method is able to accurately capture the moving boundary condition in both 2D and 3D. Fig. 9(a) and (b) show the percent mass conservation errors as a function of time for the cylinder and sphere cases, respectively. The conservation error oscillates rapidly, but is shown to be less than ±0.06% for all times. The errors for the high resolution cases are seen to oscillate less and have lower conservation errors on average. These results demonstrate that the version of the ghost–fluid method for this study accurately captures the effects of moving solid boundaries with minimal errors in conservation of mass. The error of ±0.06% is definitely a worst case scenario since the surface expansion velocities associated charring materials are much lower.

4.2. Flow over a cylinder

Fig. 10(a) shows vortex shedding behind a 1 mm diameter cylinder. A uniform mesh of 400 × 100 is used with open boundary conditions and a uniform inlet velocity of 18.9 m/s resulting in a $Re = 1000$. Figs. 10(b) shows the cross-stream velocity behind the cylinder along the centerline at 0.5 diameters downstream. A Strouhal number of $St = 0.23$ is computed and agrees well with measured values of shedding frequency of 0.22 [37,2]. Fig. 10(c) is a comparison of the computed coefficient of pressure with the results of Ref. [2] where direct numerical simulation (DNS) was used to compute the exact solution. As shown, the percent error is within 3% for all data points.

4.3. Isothermal plate heat transfer

The next validation problem considered is the heating of gas from an inclined isothermal plate as shown in Fig. 11(a). The temperature of the plate is varied to achieve a range of Rayleigh numbers and the far-field gas temperature is initialized to $T_\infty = 300$ K. Fig. 11(b) is an instantaneous temperature contour showing the transitionally turbulent nature of the flow. Fig. 11(c) is a comparison of Nusselt number, $Nu_L (= \bar{q}'' L / [(T_s - T_\infty) k_g])$ vs. Rayleigh number, $Ra_L (= \frac{g \beta (T_s - T_\infty) L^3 \cos \theta}{\nu_g \alpha_g})$ from the simulations (lines with symbols) and a standard heat transfer correlation for the lower surface of inclined plates given as [38,39],

$$Nu_L = \left[0.825 + \frac{0.387 Ra_L^{1/6}}{[1 + (0.492/Pr)^{9/16}]^{8/27}} \right]^2 \quad (26)$$

where θ is the inclination angle. The experimental data used for the Nusselt number correlation is also shown (black squares). The overall agreement is very good with a maximum difference of 8%. Additional simulations are also conducted with the mesh aligned with the fluid–solid interface and the direction of gravity modified to account for the inclination angle (green circles). The difference in Nu_L predictions and those using the immersed interface are less than 2% and is attributed to statistical errors in computing the time averaged heat flux, \bar{q}'' .

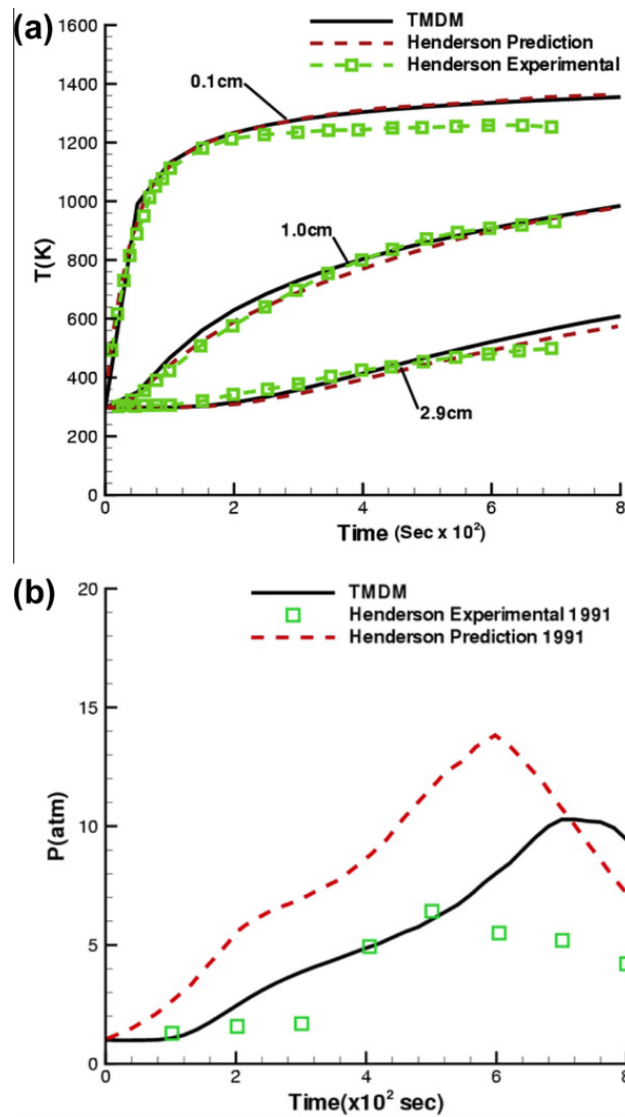


Fig. 7. Thermal model predictions showing (a) temperature and (b) gas pressure compared to experimental data [14,46,47] for a glass phenolic composite material.

4.4. Surface blowing

Errors in mass, momentum and energy exchange across the Eulerian–Lagrangian interface are important to minimize for modeling surface blowing phenomena such as flame spread. To explore the error associated with surface blowing a simple one dimensional diffusion problem is examined. The problem considered is the diffusion of one species (species A) into another species (species B) that is stagnant. The analytical expression for $Y_A(x)$ in terms of the mass fraction of species A on the interface ($Y_{A,s}$) is [40]

$$Y_A(x) = 1 - (1 - Y_{A,s}) \exp \left[\frac{Sc}{\mu(T)} \dot{m}''_A x \right]. \tag{27}$$

In the present problem, species A and B are both assumed to be nitrogen (N_2). A mass flux of $\dot{m}''_A = 1.8107 \times 10^{-3} \text{ kg/m}^2 \text{ s}$ and $Sc/\mu(T) = 38280.25 \text{ m s/kg}$ is selected to produce a surface mass fraction $Y_{A,s} = 0.5$ at $x = 0$.

Three interface methodologies are examined; “standard” ghost–fluid method, area modified ghost–fluid method, and an exact interface treatment using an Eulerian method. Fig. 12(a) compares the steady state results of the three cases against the analytical solution. Due to errors in the standard ghost–fluid method the mass fraction predicted on the interface is 0.543. This error is shown to approach 20% in Fig. 12(b) where the L^2 error norm for the three cases is provided as a function of nodes solely in the gas phase. These errors are attributed to the mass leakage across the interface discussed in detail in Section 3.2.1. Shown in the same figure, the area modified ghost–fluid and exact Eulerian methods converge first order to the analytical solution.

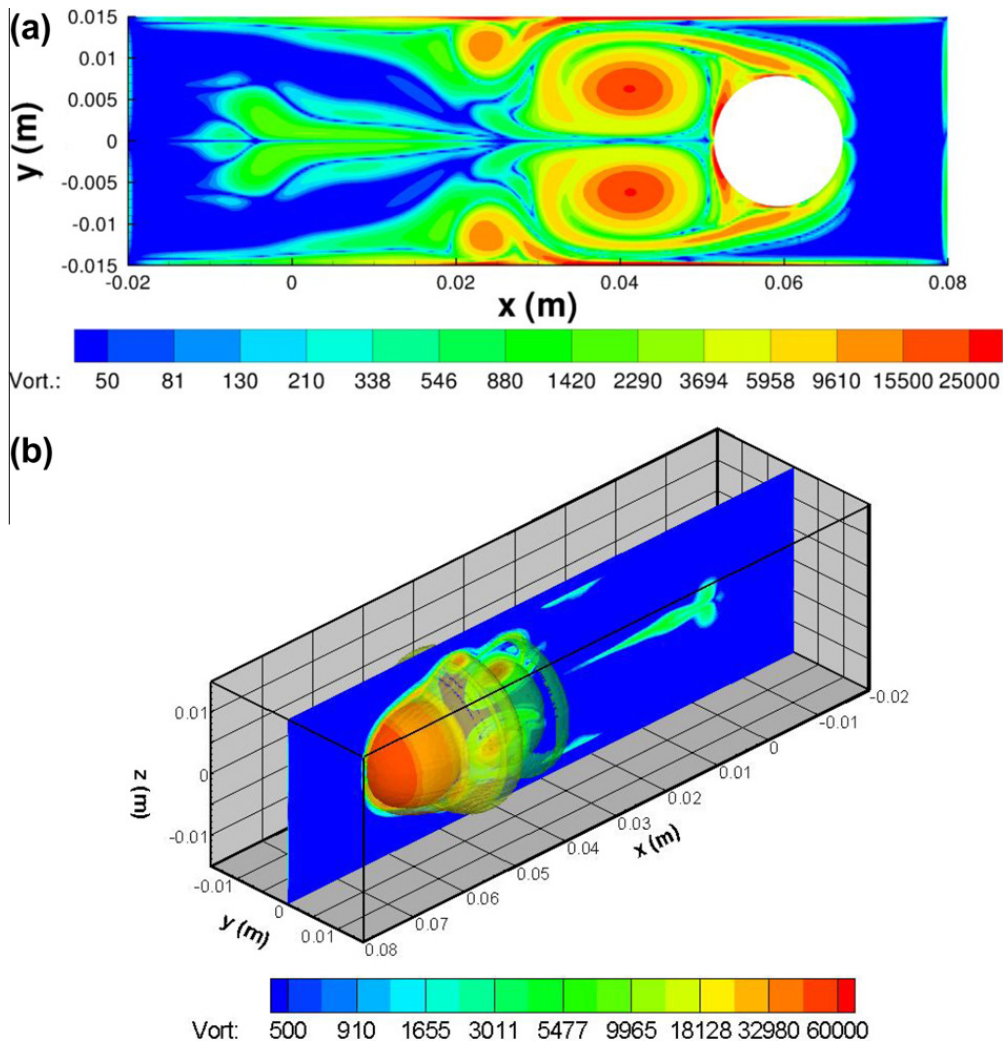


Fig. 8. Flow over a moving 2D cylinder and a 3D sphere showing (a) vorticity contours around a cylinder, and (b) vorticity contours around a sphere with an isosurface at a vorticity of 5000 and contours of density.

4.5. Sublimation with constant densities

The sublimation validation problem is chosen to test all components of the coupling algorithm which includes the moving interface and mass/energy exchange. This validation problem not only tests each of the coupling algorithms but how they interact.

The problem setup is shown in Fig. 13. The initial temperature of the domain is set equal to the solid sublimation temperature, T_s . The left boundary is then raised to T_o resulting in the generation of gas and movement of the gas/solid interface to the right. The dimensionless form of the governing equation for the gas temperature field is [41],

$$\frac{\partial^2 \theta}{\partial \eta^2} = \frac{\partial \theta}{\partial \tau} \tag{28}$$

$$\theta = \frac{T(x, t) - T_s}{T_o - T_s}, \quad \eta = x/b, \quad \tau = \alpha_g t/b^2$$

where b is a characteristic length (chosen to be the domain size) and $\alpha_g = k/(\rho C_p)$ is the thermal diffusivity. The constraints at the normalized interface location, δ , are $\theta = 0$ and $-\frac{\partial \theta}{\partial \eta} = (1/Ste) \partial \delta / \partial \tau$, where Ste is the Stefan number defined as: $Ste = C_p(T_o - T_s)/L_s$ where L_s is the heat of sublimation. The gas and solid densities are assumed identical and constant therefore there is no advection within the gas. The analytical solution for the temperature field and interface position are given by [41],

$$\theta(\eta, \tau) = 1 - \frac{\text{erf} \left[\frac{\eta}{2\sqrt{\tau}} \right]}{\text{erf}(\lambda)} \tag{29}$$

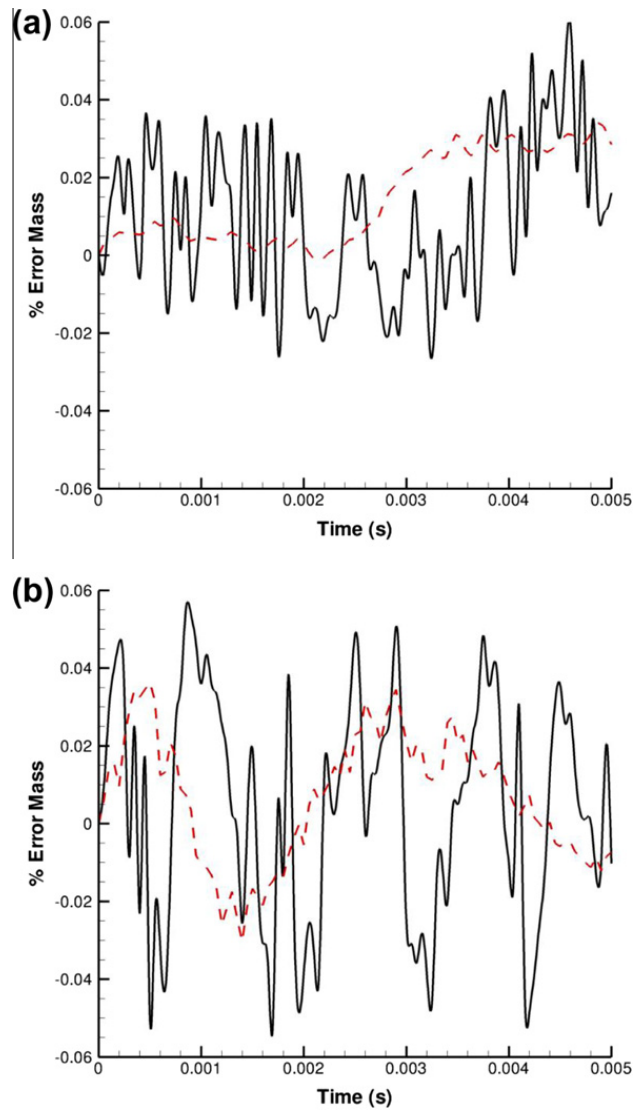


Fig. 9. Mass conservation errors for moving cylinder and sphere cases showing (a) mass conservation errors for high (dashed red) and low (black) resolution cylinder cases, and (b) mass conservation errors for high (dashed red) and low (black) resolution sphere cases. (For interpretation of the references to colour in this figure legend, the reader is referred to the web version of this article.)

$$\delta(\tau) = 2\lambda\sqrt{\tau} \tag{30}$$

where λ can be solved for numerically from the constraint equation $\sqrt{\pi}\lambda e^{\lambda^2} \text{erf}(\lambda) = St_e$.

The solid portion of the sublimation model consists of a Lagrangian mesh where the left boundary is initially at $\eta = 0$. This solid model assumes that all energy passed from the Eulerian solver (Section 3.2.2) serves to sublime the solid thereby releasing gas and moving the interface in the positive η direction. The interface velocity is calculated as: $V^I = \dot{q}'' / (\rho L_s)$. The temperature of the solid model is held at the sublimation temperature. An additional Lagrangian mesh is used to enforce the isothermal boundary condition on the left boundary of the Eulerian domain.

The sublimation problem examined is defined in terms of the parameters outlined in Table 2. The calculated interface position is compared against the analytical solution in Fig. 14(a). As the Eulerian grid is refined from a spacing of $\Delta\eta = 0.003$ to 0.114, the predicted interface location approaches the analytical solution. The rate of convergence for the interface location is shown to be nominally first order in Fig. 14(b) where the L^2 relative error norm drops from 24% to less than 1.5%. The convergence shown in Fig. 14(b) indicates that the coupling proposed algorithms not only work separately but when combined together.

4.6. Fully coupled simulations

The FE Lagrangian model discussed in Section 2.2 has been used to simulate charring of several composite systems. Most recently a decoupled study of carbon-epoxy laminates was conducted that did not include the Eulerian solver [17]. Predictions of heat release rate, time-to-ignition and final products (mass fractions, volume percentages, porosity, etc.) are compared to data given by Quintiere, Walters and Crowley (QWC) [42]. Fig. 15 shows representative results of (a)

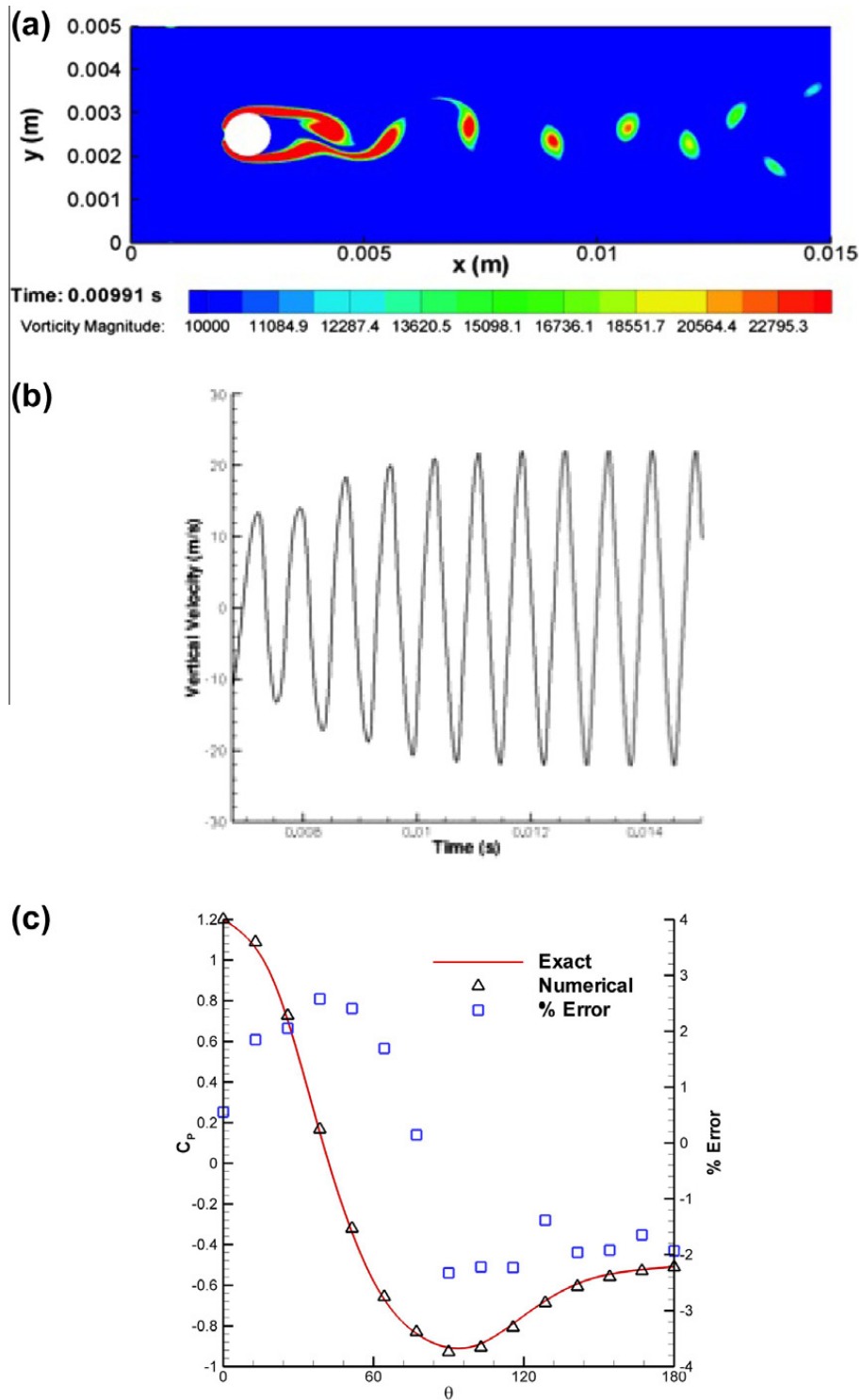
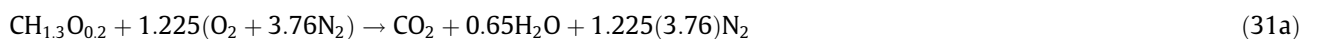


Fig. 10. Flow shedding over a stationary cylinder showing (a) Von Karman vortex streak, (b) cross-stream velocity along the centerline at 0.5 diameters downstream and (c) pressure coefficient and percent error along the upper surface (0° corresponds to the upstream stagnation point).

time-to-ignition and (b) and final products. As shown the agreement is quite good. For the present effort, the study of Ref. [17] is extended using fully coupled simulations and a mesh refinement analysis is conducted.

A single step global reaction combustion model is used to describe the gas phase combustion processes. The rate law governing reaction (31a) is specified assuming an Arrhenius relation given in Eq. (31b).



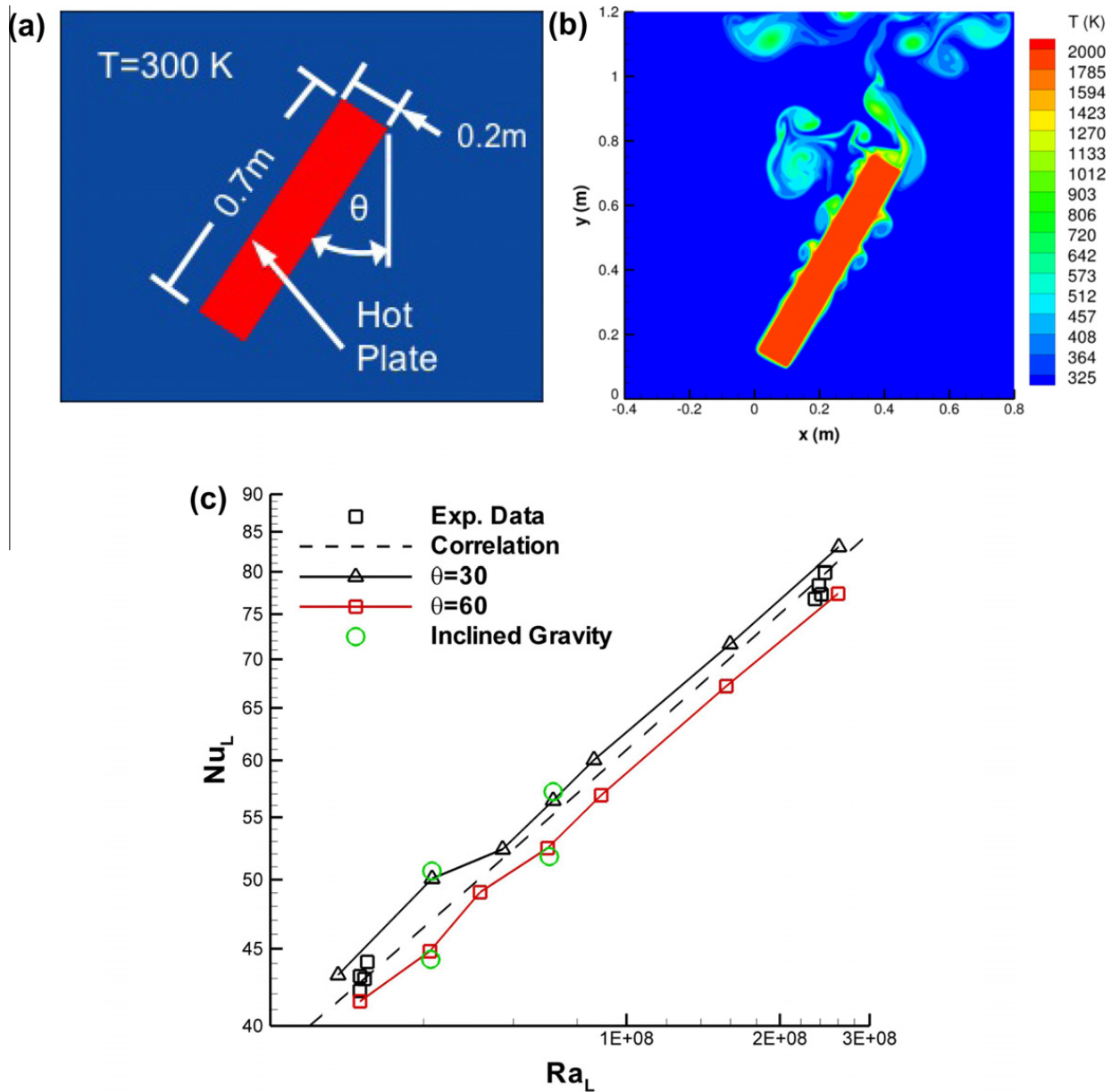


Fig. 11. Conjugate heat transfer for an isothermal plate showing (a) problem sketch, (b) instantaneous snapshot of temperature contours, (c) Nu_L vs. Ra_L for inclination angles of 30° and 60° . Green symbols are cases for which the mesh is aligned with the surface and the gravity vector changed. (For interpretation of the references to colour in this figure legend, the reader is referred to the web version of this article.)

$$\frac{d[\text{CH}_{1.3}\text{O}_{0.2}]}{dt} = -A \exp\left(\frac{-E_a}{R_u T}\right) [\text{CH}_{1.3}\text{O}_{0.2}]^{0.2} [\text{O}_2]^{1.3} \quad (31b)$$

The resulting system of ordinary differential equations is simultaneously solved using a customized version of the Semi-Implicit Euler numeric integrator found in Ref. [43]. As an approximation proportions of carbon, hydrogen and oxygen in the pyrolysis gas are assumed to be the same as those given by Tewarson as $\text{CH}_{1.3}\text{O}_{0.2}$ [44]. The reaction in Eq. (31a) is chosen to be similar to that for methane where the Arrhenius parameters are obtained from Ref. [45]. Further details on the treatment of the epoxy gas is available in Ref. [17].

A mesh refinement study of the fully coupled problem outlined in Fig. 16 is performed in both one and two dimensions. The two dimensional problem setup consists a $2.5\text{ cm} \times 5.0\text{ m}$ fluid domain. The inset in Fig. 16 provides the detail of the $3.2\text{ mm} \times 2\text{ cm}$ carbon epoxy sample composed of 8×50 elements. A circular ignition source, placed at $1.0\text{ cm} \times 0.75\text{ cm}$ with a surface temperature of 900 K , serves to initially ignite the gas released from the composite. The one dimensional cases are equivalent to a slice taken at $y = 1.5\text{ cm}$ from the two dimensional problem. Consistent with the analysis described in Ref. [17], two additional heat fluxes are applied to the left hand side of the sample. The first is a uniform background heat flux of 25 kW/m^2 (from a radiant heating panel) and the second is an ignition heat flux of 60 kW/m^2 over the lower quarter of the sample as indicated in Fig. 16 (to account for burner induced ignition).

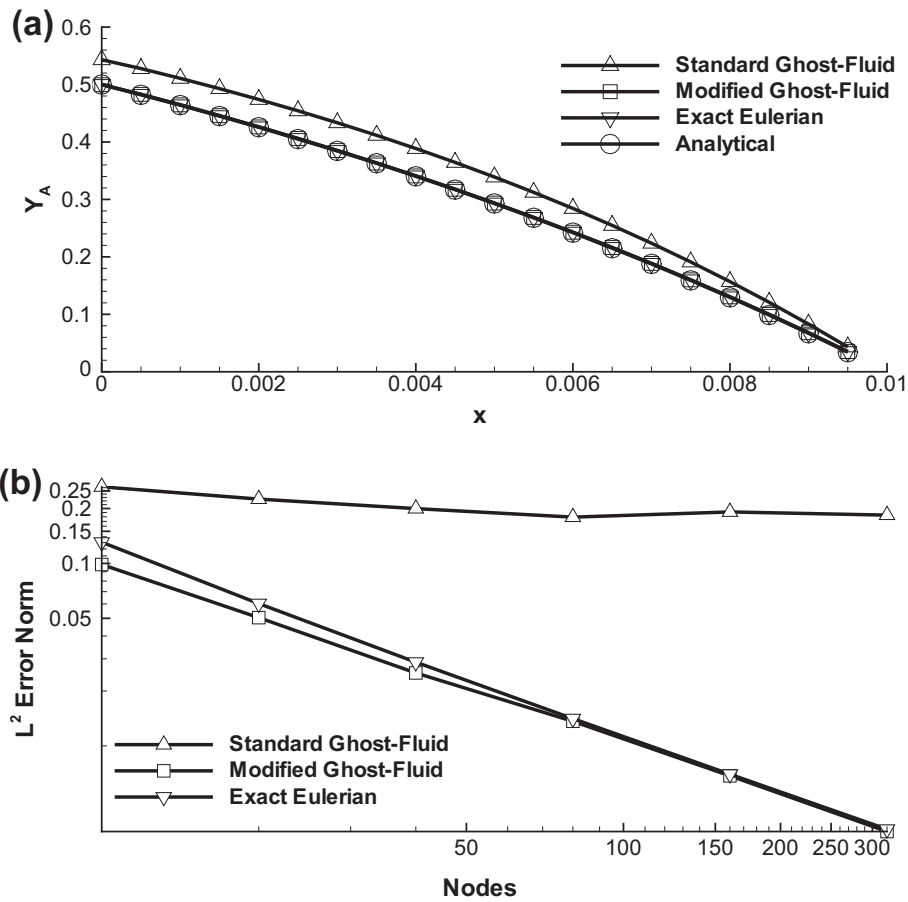


Fig. 12. One-dimensional diffusion test problem results showing (a) steady state mass fraction distribution and (b) L^2 error for the “standard” ghost–fluid method, area modified ghost–fluid method, and exact interface treatment using an Eulerian method.

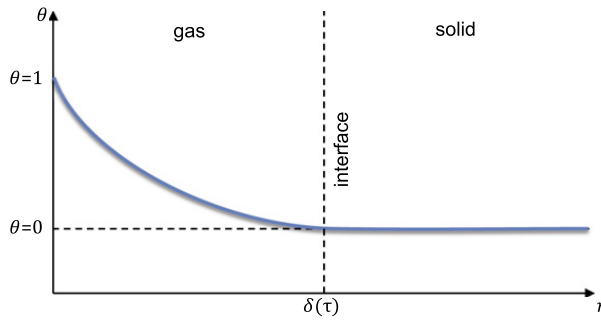


Fig. 13. A sketch of the sublimation validation problem of Section 4.5.

Table 2
The parameters used to define sublimation validation problem.

| Parameter | Value |
|-------------|--|
| Ste | 0.0674 |
| α_g | $6.88 \times 10^{-6} \text{ m}^2/\text{s}$ |
| $T_o - T_s$ | 5 K |

The convergence analysis is performed by varying the number of Eulerian nodes from a spacing of 0.5 mm to 0.016 mm for the 1D cases and 1.0 mm to 0.125 mm for the 2D cases. Since an exact solution is not available, the most refined case is chosen as the basis for the L^2 relative error norm. Two parameters are utilized to study convergence, the total heating rate (\dot{Q}) and average surface temperature. The total heat is calculated as $\dot{Q} = \int_{\Gamma} (\dot{q}) d\Gamma$. The area of interest (Γ) for both param-

eters is limited to the left hand side of the panel. The rate of convergence for both parameters is shown to be nominally first order in Fig. 17 where there is clear overlap between the 1D and 2D L^2 relative error norms. The error associated with average surface temperature is approximately two orders of magnitude less than that of total heat error. As described in Section 3.2.2, the heat flux is calculated based upon the gradients of temperature thereby introducing additional error to that of the temperature field. The convergence shown in Fig. 17 indicates that the coupling proposed algorithms not only work separately but when combined together.

Fig. 18 illustrates the typical progression of heating, composite pyrolysis, and combustion. As shown in Fig. 18(a), the lower region of the composite first decomposes from the applied heat load thereby releasing volatile gases indicated with the mass fraction of $\text{CH}_{1.3}\text{O}_{0.2}$. When the volatile gases and available oxygen reach the ignition temperature they ignite. The flame shortly after ignition is shown in Fig. 18(b). This flame increases the overall heat returned to the surface causing additional pyrolysis and volatile gas release shown in Fig. 18(c). The pyrolysis of the composite material is accompanied by expansion also shown in this figure. As the pyrolysis region grows from the additional heat from the flame the primary mechanism of flame spread is modeled.

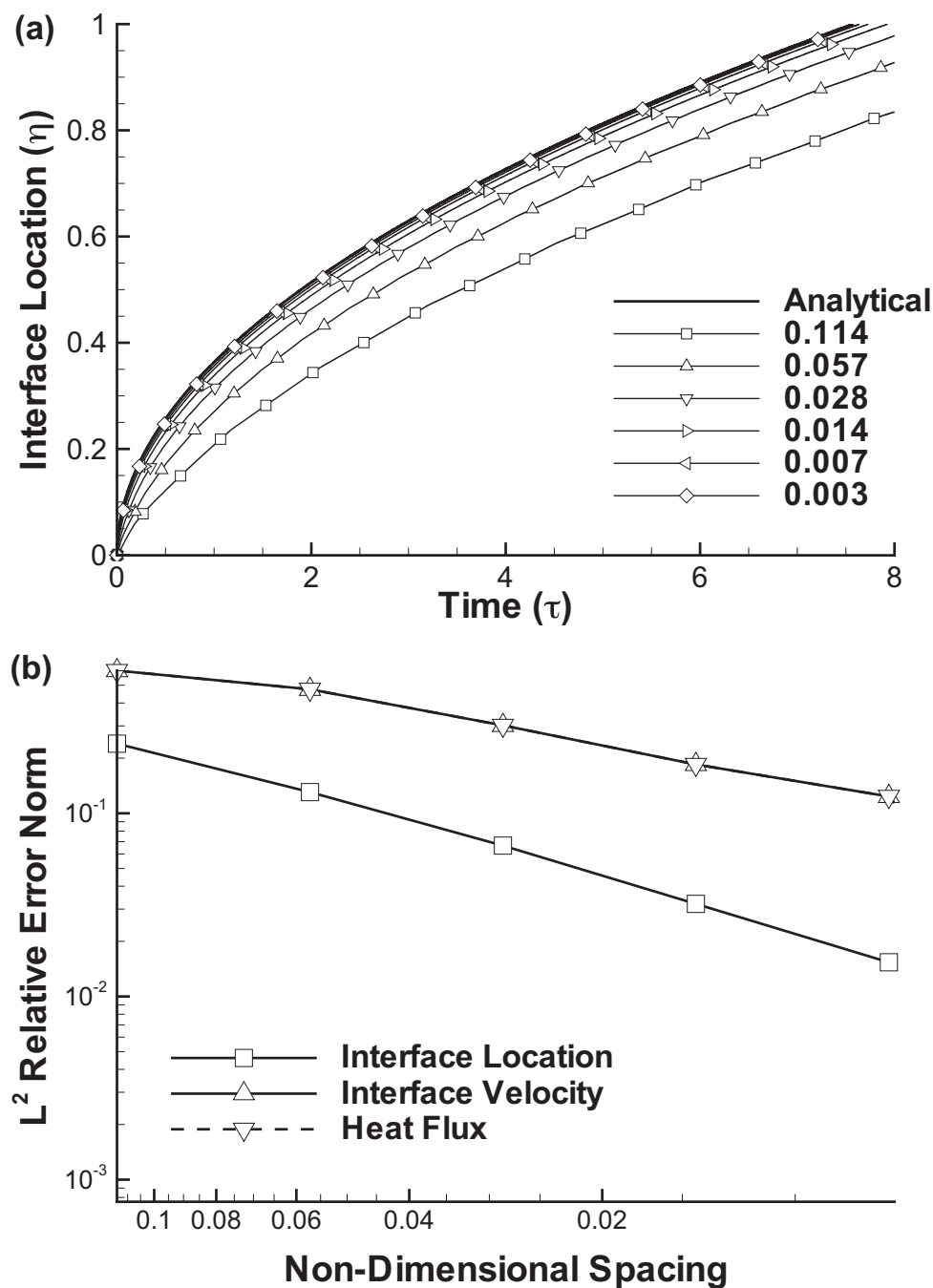


Fig. 14. One-dimensional sublimation test problem results showing (a) the predicted interface location with grid refined compared to the analytical solution and (b) L^2 relative error norm for the non-dimensional interface location, velocity, and heat flux.

5. Conclusions

An immersed boundary methodology for the modeling of conjugate heat and mass transfer is presented with specific application to fire environments. The model addresses the need for an efficient and accurate update of the moving interfaces, a no-slip and no-penetration solid interface and exchange of energy and mass transfer across the interfaces. The need for an efficient and accurate interface update is accomplished with the introduction of a patch system which systematically reduces the resolution of the Lagrangian model as a function of distance from the interface. A combination of ghost–fluid approaches and point source forcing functions at the interface are used to impose the last two constraints.

This methodology is shown to satisfy conservation principles with minimal error. Further validation is performed with modeling of flow over a cylinder with excellent results. The heat transfer aspect of the methodology is verified with an isothermal plate in buoyancy driven flow. The surface blowing case verified the need for area modification in the ghost–fluid method in order to accurately capture low speed flows. Lastly, the newly introduced immersed interface methodology is utilized to study the burning of carbon-epoxy composites along with a convergence analysis.

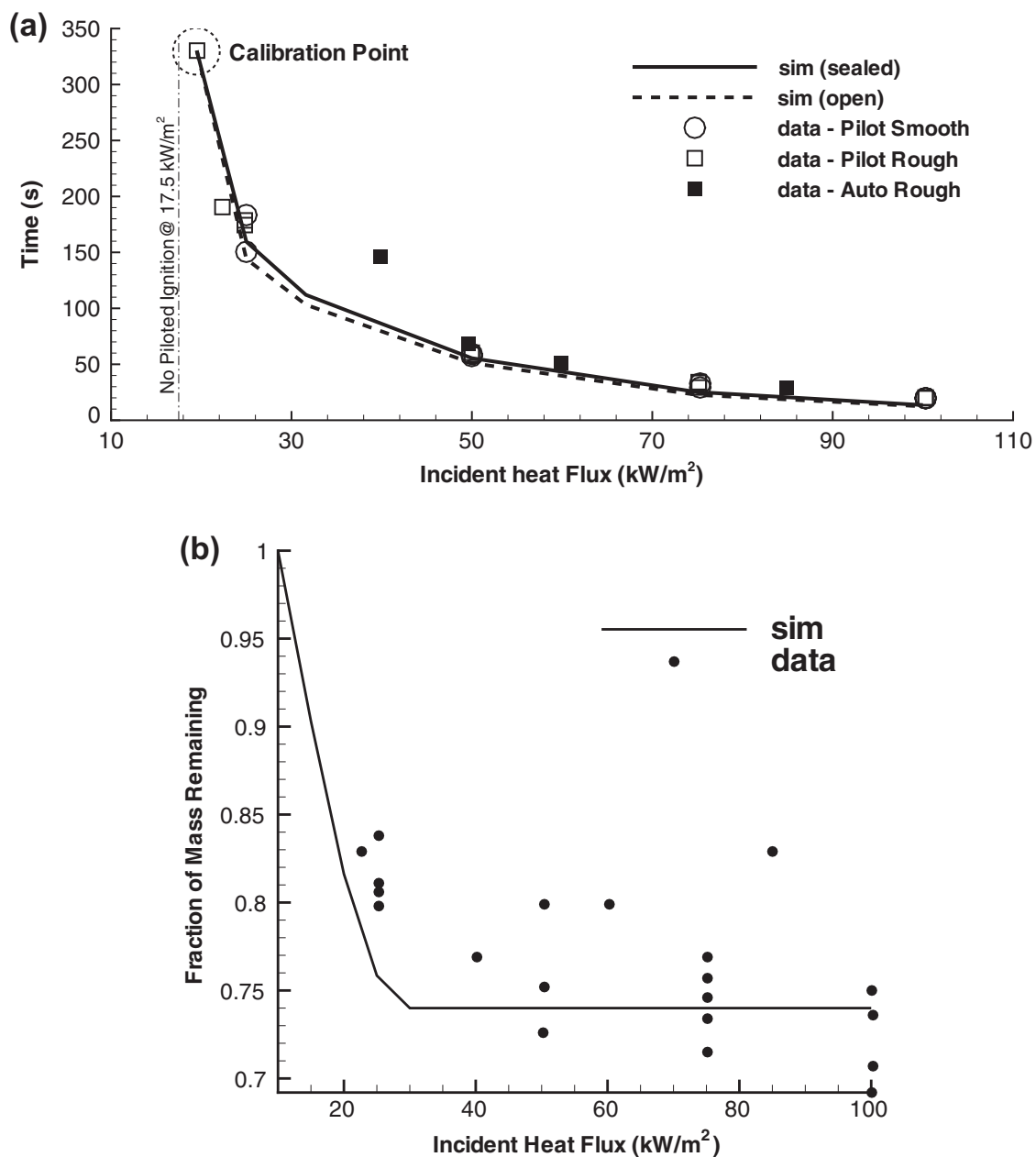


Fig. 15. Carbon-epoxy composite simulations from Ref. [17] compared to the experimental results of Quintiere, Walters and Crowley [42] where (a) is time-to-ignition with simulated sealed and open right boundaries and (b) final product predictions of V/V_o , V_g/V_e and Y_{rc} with increasing incident heat flux.

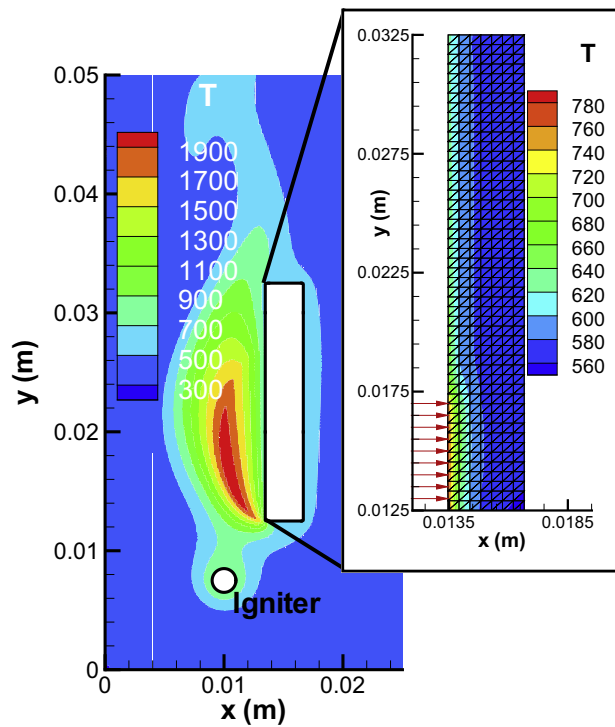


Fig. 16. Fully coupled simulation showing the CFD and FE domains along with igniter.

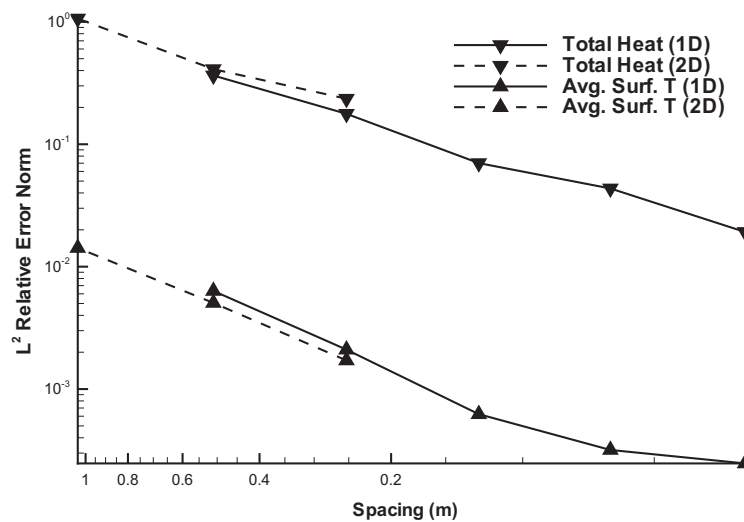


Fig. 17. The L^2 relative error norm in average surface temperature and total heat to the surface for the fully coupled simulations in one and two dimensions.

Acknowledgements

This research was supported by the Office of Naval Research under Grants N00014-06-1-0623 and N00014-08-C-0591 and by the National Science Foundation (NSF) under grant CBET-1033328.

References

- [1] C.S. Peskin, Flow patterns around heart valves: a numerical method, *J. Comput. Phys.* 10 (1972) 252–271.
- [2] Y. Tseng, J.H. Ferziger, A ghost-cell immersed boundary method for flow in complex geometry, *J. Comput. Phys.* 192 (2003) 593–623.
- [3] D. Lacanette, S. Vincent, A. Sarthou, P. Malaurent, J.-P. Caltagirone, An eulerian/lagrangian method for the numerical simulation of incompressible convection flows interacting with complex obstacles: Application to the natural convection in the lascaux cave, *Int. J. Heat Mass Transfer* 52 (2009) 2528–2542.
- [4] T. G. Liu, B. C. Khoo, Y. S. Yeo, Ghost fluid method for strong shock impacting on material interface, *J. Comput. Phys.* 190 (2003) 651–681.

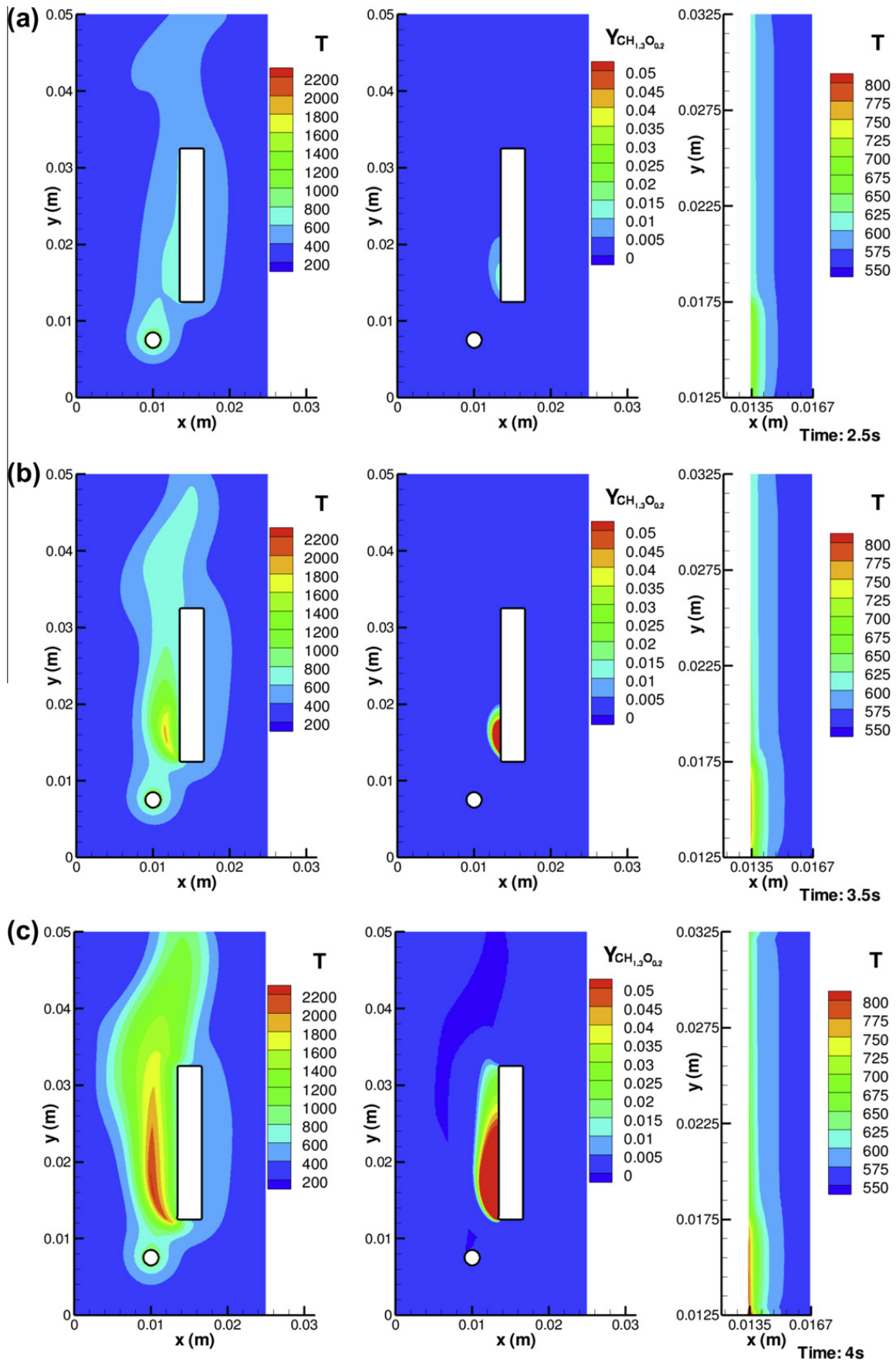


Fig. 18. Fully coupled simulations of the carbon-epoxy composite showing mass fraction of $\text{CH}_{1.3}\text{O}_{0.2}$, gas and composite temperatures after (a) 2.5 s, (b) 3.5 s and (c) 4 s.

- [5] C. Wag, H. Tang, T. Liu, An adaptive ghost fluid finite volume method for compressible gas-water simulations, *J. Comput. Phys.* 227 (2008) 6385–6409.
- [6] C. Farhat, A. Rallu, S. Shankaran, A higher-order generalized ghost fluid method for the poor for the three-dimensional two-phase flow computation of underwater implosions, *J. Comput. Phys.* 227 (2008) 7674–7700.
- [7] C. Farhat, A. Rallu, K. Wang, T. Belytschko, Robust and provably second-order explicit and implicit staggered time-integrators for highly non-linear compressible fluid-structure interaction problems, *Int. J. Numer. Meth. Eng.* 84 (2010) 73–107.
- [8] S. Osher, R. Fedkiw, *Level set methods and dynamic implicit surfaces*, Springer, New York, 2003.
- [9] R. Mittal, G. Iaccarino, Immersed boundary methods, *Ann. Rev. Fluid Mech.* 37 (2005) 239–261.
- [10] W. Xie, P.E. DesJardin, A level set embedded interface method for conjugate heat transfer simulations of low speed 2d flows, *Comput. Fluids* 37 (2008) 1262–1275.
- [11] W. Xie, P. DesJardin, An embedded upward flame spread model using 2d direct numerical simulations, *Combust. Flame* 156 (2009) 522–530.
- [12] F.M. White, *Viscous Fluid Flow*, McGraw-Hill, Inc., New York, NY, 1991.
- [13] A. Mouritz, S. Feih, E. Kandare, Z. Mathys, A.G. Gibson, P. DesJardin, S.W. Case, B.Y. Lattimer, Review of fire structural modelling of polymer composites, *Composites* 40 (2009) 1800–1814.
- [14] C. Luo, P.E. DesJardin, Thermo-mechanical damage modeling for a glass-fiber phenolic-resin composite material, *Compos. Sci. Technol.* 67 (2007) 1475–1488.
- [15] S.K. Sambasivan, H. Udaykumar, Ghost fluid method for strong shock interactions part 2: Immersed solid boundaries, *AIAA J.* 47 (2009) 2923–2937.
- [16] C. Luo, W. Xie, P. DesJardin, Fluid-structure simulations of composite material response for fire environments, in: L. Couchman, A. Moritz (Eds.), *Modeling of Naval Composite Structures in Fire*, 2006, pp. 255–279.
- [17] M.T. McGurn, P.E. DesJardin, A.B. Dodd, Numerical simulation of expansion and charring of carbon-epoxy laminates in fire environments, *Int. J. Heat Mass Transfer* 55 (2012) 272–281.
- [18] P.E. DesJardin, T.J. O'Hern, S.R. Tieszen, Large eddy simulation and experimental measurements of the near-field of a large turbulent helium plume, *Phys. Fluids* 16 (2004) 1866–1883.
- [19] P.E. DesJardin, Modeling of conditional dissipation rate for flamelet models with application to large eddy simulation of fire plumes, *Combust. Sci. Technol.* 177 (2005) 1881–1914.
- [20] P. DesJardin, H. Shih, M. D. Carrara, State-of-the-art combustion sgs modeling approaches for large eddy simulation of fires, in: B. Sunden, M. Faghri (Eds.), *Transport Phenomena of Fires*, WIT Press, UK, Southampton, UK, 2008, pp. 327–356.
- [21] J.A. Sethian, *Level Set Methods and Fast Marching Methods*, Cambridge University Press, Cambridge, UK, 1999.
- [22] M. Sussman, P. Smereka, S. Osher, A level set approach for computing solutions to incompressible two-phase flow, *J. Comput. Phys.* 114 (1994) 146–159.
- [23] S. Mauch, *Efficient algorithms for solving static Hamilton–Jacobi equations*, Ph.D. thesis, California Institute of Technology, 2003.
- [24] S. Xu, T. Aslam, D.S. Stewart, High resolution numerical simulation of ideal and non-ideal compressible reacting flows with embedded internal boundaries, *Combust. Theory Modell.* 1 (1997) 113–142.
- [25] R.K. Fedkiw, T. Aslam, B. Merriman, S. Osher, A non-oscillatory eulerian approach to interfaces in multimaterials flows (the ghost fluid method), *J. Comput. Phys.* 152 (1999) 457–492.
- [26] R. Fedkiw, Coupling an Eulerian fluid calculation to a Lagrangian solid calculation with the ghost fluid method, *J. Comput. Phys.* 175 (2002) 200–224.
- [27] M. Arienti, P. Hung, E. Morano, J.E. Shepherd, A level set approach to Eulerian–Lagrangian coupling, *J. Comput. Phys.* 185 (2003) 213–251.
- [28] T. Ye, R. Mittal, H. Udaykumar, W. Shyy, An accurate cartesian grid method for viscous incompressible flows with complex immersed boundaries, *J. Comput. Phys.* 156 (1999) 209–240.
- [29] G.S. James, *A Brief on Tensor Analysis*, Undergraduate Texts in Mathematics, Springer-Verlag, New York, 1994.
- [30] M.-S. Liou, A sequel to ausm: Ausm+, *J. Comput. Phys.* 129 (1996) 364–382.
- [31] M.-S. Liou, A sequel to ausm, part ii: Ausm+up for all speeds, *J. Comput. Phys.* 214 (2006) 137–170.
- [32] Y. Li, Wavenumber-extended high-order upwind-biased finite-difference schemes for convective scalar transport, *J. Comput. Phys.* 133 (1997) 235–255.
- [33] C.-W. Shu, S. Osher, Efficient implementation of essentially non-oscillatory shock-capturing schemes, *J. Comput. Phys.* 77 (1988) 364–382.
- [34] M. Baker, B. Carpenter, A. Shafi, *MPJ Express: Towards Thread Safe Java HPC*, in: *IEEE International Conference on Cluster Computing (Cluster 2006)*, Barcelona, Spain, 2006.
- [35] C. Farhat, P.-S. Chen, F. Risler, F.-X. Roux, Unified framework for accelerating the convergence of iterative substructuring methods with lagrange multipliers, *Int. J. Numer. Meth. Eng.* 42 (1998) 257–288.
- [36] L.N. Trefethen, D. Bau, *Numerical linear algebra*, Society for Industrial and Applied Mathematics, Philadelphia, 1997.
- [37] U. Fey, M. Konig, H. Eckelmann, A new Strouhal–Reynolds number relationship for circular cylinder in the range $47 < Re < 2 \times 10^5$, *Phys. Fluids* 19 (1998) 1547–1550.
- [38] F.P. Incopera, D.D.P., *Fundamentals of Heat and Mass Transfer*, John Wiley & Sons, New York, NY, 1990.
- [39] B.R. Rich, An investigation of heat transfer from an inclined flat plate in free convection, *Trans. ASME* 75 (1953) 489–499.
- [40] S.R. Turns, *An Introduction to Combustion*, McGraw-Hill, Inc., New York, NY, 1996.
- [41] M.N. Ozisik, *Heat Conduction*, second ed., Wiley-Interscience Publication, Wiley, New York, NY, 1993.
- [42] J.G. Quintiere, R.N. Walters, S. Crowley, *Flammability Properties of Aircraft Carbon-Fiber Structural Composite*, Technical Report DOT/FAA/AR-07/57, US Department of Transportation, Federal Aviation Administration, 2007.
- [43] W. Press, S. Teukolsky, W. Vetterling, B. Flannery, *Numerical Recipes: The Art of Scientific Computing*, Cambridge University Press, 2007.
- [44] A. Tewarson, Generation of heat and chemical compounds in fires, in: P. DiNenno (Ed.), *The SFPE Handbook of Fire Protection Engineering*, National Fire Protection Association, 2002, pp. 3–82–3–161.
- [45] C. Westbrook, F. Dryer, Simplified reaction mechanisms for the oxidation of hydrocarbon fuels in flames, *Combust. Sci. Technol.* 27 (1981) 31–43.
- [46] J.B. Henderson, J.A. Wiebelt, M.R. Tant, A model for the thermal response of polymer composite materials with experimental verification, *J. Compos. Mater.* 19 (1985) 579–595.
- [47] J.B. Henderson, T.E. Wiecek, A mathematical model to predict the thermal response of decomposing expanding polymer composites, *J. Compos. Mater.* 21 (1987) 373–393.